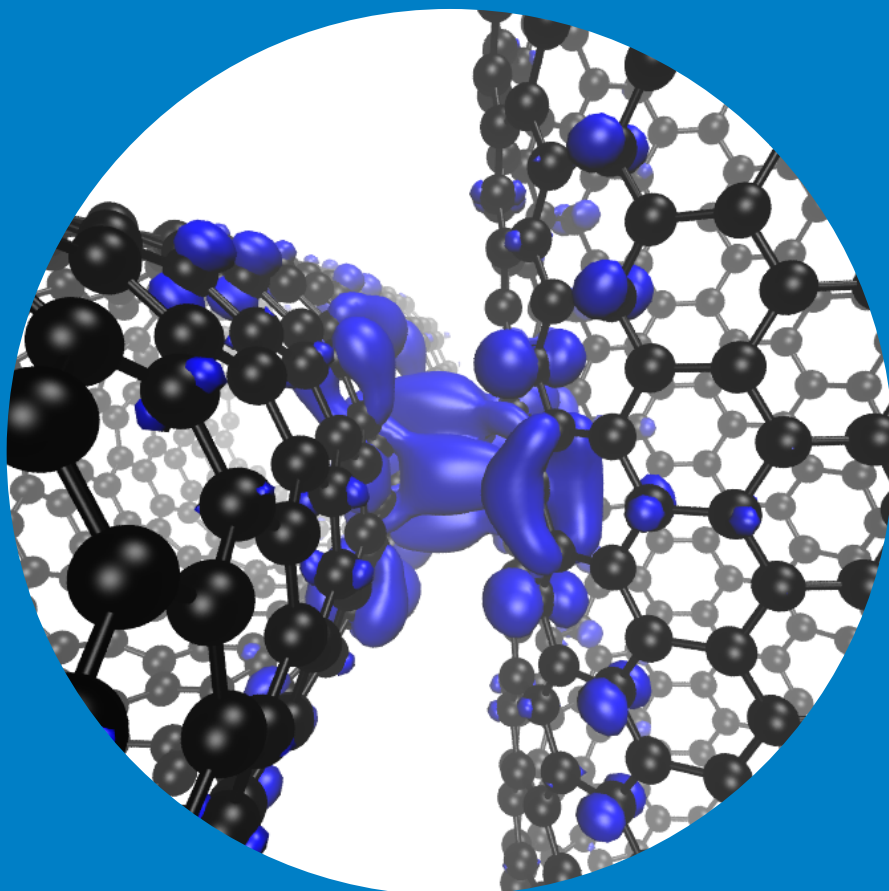


Department of Applied Physics

Electrical conductivity of functionalised carbon nanotube networks

Tomi Ketolainen



Electrical conductivity of functionalised carbon nanotube networks

Tomi Ketolainen

A doctoral dissertation completed for the degree of Doctor of Science (Technology) to be defended, with the permission of the Aalto University School of Science, at a public examination held at the lecture hall M1 of the school on the 8th of February, 2019 at 13 o'clock.

Aalto University
School of Science
Department of Applied Physics
Electronic Properties of Materials

Supervising professor

Prof. Martti Puska, Aalto University, Finland

Thesis advisor

Dr. Ville Havu, Aalto University, Finland

Preliminary examiners

Dr. Jouko Nieminen, Tampere University of Technology, Finland

Dr. Christoph Scheurer, Technical University of Munich, Germany

Opponent

Prof. Mads Brandbyge, Technical University of Denmark, Denmark

Aalto University publication series

DOCTORAL DISSERTATIONS 12/2019

© 2019 Tomi Ketolainen

ISBN 978-952-60-8383-4 (printed)

ISBN 978-952-60-8384-1 (pdf)

ISSN 1799-4934 (printed)

ISSN 1799-4942 (pdf)

<http://urn.fi/URN:ISBN:978-952-60-8384-1>

Unigrafia Oy

Helsinki 2019

Finland

Publication orders (printed book):

tomi.ketolainen@aalto.fi



Printed matter
4041-0619

Author

Tomi Ketolainen

Name of the doctoral dissertation

Electrical conductivity of functionalised carbon nanotube networks

Publisher School of Science**Unit** Department of Applied Physics**Series** Aalto University publication series DOCTORAL DISSERTATIONS 12/2019**Field of research** Engineering Physics, Theoretical and Computational Physics**Manuscript submitted** 8 October 2018**Date of the defence** 8 February 2019**Permission to publish granted (date)** 29 November 2018**Language** English **Monograph** **Article dissertation** **Essay dissertation****Abstract**

The fabrication of novel electronic devices requires new kinds of materials. The use of carbon nanotubes (CNTs) in various applications has already been demonstrated and therefore the CNTs are also important carbon materials in addition to graphene and fullerenes. Because the electronic properties of individual CNTs depend on their atomic structures, the individual CNTs are not possibly the best choice for building new electronics. Instead, the new devices could be made using thin films or networks of CNTs. The CNT thin films are transparent, flexible, and conduct electricity. Hence, the CNT thin films are expected to be utilised in a remarkable amount of applications including transistors, touch screens, and solar cells. However, a significant challenge related to the CNT thin films is making a film with both high conductivity and transparency simultaneously.

Several methods to improve the conductivity of CNT networks have been studied experimentally. The goal of this thesis is to investigate a few methods to increase the conductivity of CNT networks by using density functional theory combined with the standard Green's function electron transport calculations. In particular, the conductance of junctions of CNTs is examined since the CNT junctions mainly determine the conductivity of the whole network.

Two different approaches to improve the electrical conductivity of CNT networks are studied. The conductivity can be enhanced by depositing group 6 transition metal (TM) atoms on the CNT networks because the TM atoms are able to link the CNTs. The four-terminal electron transport calculations show that Cr, Mo, and W linker atoms enhance the conductances of the CNT junctions in a similar way. The increase in the conductance is related to the strong hybridisation between the carbon and TM atom orbitals. The second approach is based on functionalising the CNTs with molecules. The interaction of AuCl₄ molecules with CNTs leads to a p-type doping effect. In addition, the doping of CNTs with nitric acid is studied and the NO₃ molecules also cause a p-type doping effect in CNTs. Interestingly, the doping effect is larger in semiconducting CNTs than in metallic ones. Moreover, water molecules near the NO₃ molecules enhance the doping effect. The electron transport through the CNT junctions can be increased by doping the CNTs with AuCl₄ or NO₃ molecules and no linker molecule is needed if the concentration of the molecules on the CNTs is high enough. A central result is the pinning of the Fermi level to the van Hove singularities and flat molecular states. The results of our work also improve the understanding of previous experimental studies.

Keywords Density functional theory, electronic transport, carbon nanotubes**ISBN (printed)** 978-952-60-8383-4**ISBN (pdf)** 978-952-60-8384-1**ISSN (printed)** 1799-4934**ISSN (pdf)** 1799-4942**Location of publisher** Helsinki**Location of printing** Helsinki **Year** 2019**Pages** 118**urn** <http://urn.fi/URN:ISBN:978-952-60-8384-1>

Tekijä

Tomi Ketolainen

Väitöskirjan nimi

Funktionalisoitujen hiilinanoputkiverkkojen sähkönjohtavuus

Julkaisija Perustieteiden korkeakoulu**Yksikkö** Teknillisen fysiikan laitos**Sarja** Aalto University publication series DOCTORAL DISSERTATIONS 12/2019**Tutkimusala** Teknillinen fysiikka, teoreettinen ja laskennallinen fysiikka**Käsikirjoituksen pvm** 08.10.2018**Väitöspäivä** 08.02.2019**Julkaisuluvan myöntämispäivä** 29.11.2018**Kieli** Englanti **Monografia** **Artikkeliväitöskirja** **Esseeväitöskirja****Tiivistelmä**

Uusien elektronisten laitteiden valmistus vaatii uudenlaisia materiaaleja. Hiilinanoputkien käyttäminen useissa sovelluksissa on jo demonstroitu, ja siksi hiilinanoputket ovat myös tärkeitä hiilimateriaaleja grafeenin ja fulleriinien lisäksi. Koska yksittäisten hiilinanoputkien elektroniset ominaisuudet riippuvat hiilinanoputkien atomirakenteesta, yksittäiset hiilinanoputket eivät mahdollisesti ole paras valinta uuden elektronikan rakentamista varten. Sen sijaan uusia laitteita voitaisiin valmistaa käyttäen hiilinanoputkiohukalvoja tai -verkkoja. Hiilinanoputkiohukalvot ovat läpinäkyviä, taipuisia ja johtavat sähköä. Siksi hiilinanoputkiohukalvoja odotetaan hyödynnettävänä merkittävässä määrässä sovelluksia mm. transistoreissa, kosketusnäyttöissä ja aurinkokennoissa. Merkittävä hiilinanoputkiohukalvoihin liittyvä haaste on kuitenkin valmistaa kalvo, jolla on samanaikaisesti sekä suuri johtavuus että läpinäkyvyys.

Useita menetelmiä hiilinanoputkiverkkojen johtavuuden parantamiseen on tutkittu kokeellisesti. Tämän tutkielman tavoite on selvittää muutamaa menetelmää hiilinanoputkiverkkojen johtavuuden parantamista varten käyttäen tiheysfunktionaaliteoriaa yhdistettynä tavallisiin Greenin funktio -elektronikuljetuslaskuihin. Erityisesti hiilinanoputkiliitosten johtavuutta tutkitaan, koska hiilinanoputkiliitokset pääasiassa määrittävät koko verkon johtavuuden.

Kahta erilaista lähestymistapaa hiilinanoputkiverkkojen sähkönjohtavuuden parantamiseksi tutkitaan. Johtavuutta voidaan kasvattaa pinnoittamalla hiilinanoputkiverkot ryhmän 6 transitiometalliatomeilla, koska transitiometalliatomit pystyvät yhdistämään hiilinanoputket. Neljän terminaalien elektronikuljetuslaskut osoittavat, että Cr-, Mo- ja W-linkkeriatomit voimistavat hiilinanoputkiliitosten johtavuutta samalla tavalla. Johtavuuden kasvu liittyy vahvaan hybridisaatioon hiili- ja transitiometalliatomien orbitaalien välillä. Toinen lähestymistapa perustuu hiilinanoputkien funktionalisoimiseen molekyyileillä. Vuorovaikutus AuCl₄-molekyylien ja hiilinanoputkien välillä johtaa p-tyyppin douppausefektiin. Lisäksi tutkitaan hiilinanoputkien douppausta typpihapolla, ja NO₃-molekyylit aiheuttavat myös p-tyyppin douppausefektin hiilinanoputkissa. Douppausefekti on mielenkiintoisella tavalla suurempi puolijohtavissa hiilinanoputkissa kuin metallisissa. Lisäksi vesimolekyylit NO₃-molekyylien lähellä voimistavat douppausefektia. Elektronien kuljetusta hiilinanoputkiliitosten läpi voidaan kasvattaa douppaamalla hiilinanoputket AuCl₄- tai NO₃-molekyyleillä, eikä linkkerimolekyyliä tarvita, jos molekyylien konsentraatio hiilinanoputkilla on tarpeeksi suuri. Keskeinen tulos on Fermi-tason kiinnittyminen van Hove -singulariteetteihin ja tasaisiin molekyyliiloihin. Työmme tulokset parantavat myös aikaisempien kokeellisten tutkimusten ymmärtämystä.

Avainsanat Tiheysfunktionaaliteoria, elektronien kuljetus, hiilinanoputket**ISBN (painettu)** 978-952-60-8383-4**ISBN (pdf)** 978-952-60-8384-1**ISSN (painettu)** 1799-4934**ISSN (pdf)** 1799-4942**Julkaisupaikka** Helsinki**Painopaikka** Helsinki**Vuosi** 2019**Sivumäärä** 118**urn** <http://urn.fi/URN:ISBN:978-952-60-8384-1>

Preface

This thesis presents my research work that I have carried out in the Electronic Properties of Materials group at the Aalto University. First, I would like to thank Prof. Martti Puska for working as a supervisor for me. His advice and encouragement have been important to me during the time when I have started to work on new and challenging topics. In addition, I want to thank my thesis advisor Dr. Ville Havu for good discussions we have had together. Because this kind of work is often done in a research group, I also want to thank all current and former students, post-doc researchers, and senior researchers who have been in our group. In particular, I have enjoyed the common time that we have had in several scientific meetings and free-time events. The inspiring discussions with Prof. Esko Kauppinen and Prof. Kari Laasonen have also been useful. Furthermore, I am grateful to Prof. František Karlický for giving me an opportunity to start to work in his group while finishing this thesis.

I am also thankful to my Mom, Dad, and sister for sharing their time with me. It has been great to have good conversations and to have common activities. All these things have also been nice and significant for me.

Helsinki, January 2, 2019,

Tomi Ketolainen

Contents

| | |
|--|------------|
| Preface | i |
| List of Publications | iii |
| Author's Contribution | v |
| 1. Introduction | 1 |
| 2. Basic ideas of density functional theory | 3 |
| 2.1 Schrödinger equation and the wavefunction | 3 |
| 2.2 Determining the electron density | 4 |
| 2.3 Exchange-correlation functionals | 5 |
| 2.4 Hybrid exchange-correlation functionals | 8 |
| 2.5 Including the van der Waals correction and overview of the FHI-aims code package | 9 |
| 3. Computing transmission functions | 13 |
| 3.1 Conductance of a nanoscale device | 13 |
| 3.2 Transport system | 14 |
| 3.3 Numerical calculation of the transmission function | 17 |
| 4. Carbon nanotube thin films | 21 |
| 4.1 Conductivity of the carbon nanotube network | 22 |
| 4.2 Acid doping | 24 |
| 4.3 Other common dopants and methods to modify the properties of carbon nanotube thin films | 26 |
| 5. Carbon nanotube junctions with linker atoms | 31 |
| 5.1 Structure of the CNT junction | 32 |
| 5.2 Electronic transmission functions and charge densities | 33 |
| 6. Molecular doping of carbon nanotubes and carbon nanotube junctions | 37 |
| 6.1 Semiconducting carbon nanotubes with AuCl ₄ molecules | 37 |
| 6.2 Carbon nanotubes with NO ₃ molecules | 47 |
| 6.3 Junctions of CNTs doped with NO ₃ molecules | 54 |
| 7. Conclusions | 61 |
| References | 63 |
| Publications | 69 |

List of Publications

This thesis consists of an overview and of the following publications which are referred to in the text by their Roman numerals.

I T. Ketolainen, V. Havu, and M. J. Puska. Enhancing conductivity of carbon nanotube networks by transition metal adsorption. *The Journal of Chemical Physics*, 142, 054705, February 2015.

II T. Ketolainen, V. Havu, and M. J. Puska. Conductivity of AuCl₄-Functionalized Carbon Nanotube Networks. *The Journal of Physical Chemistry C*, 121, 4627, March 2017.

III T. Ketolainen, V. Havu, E. Ö. Jónsson, and M. J. Puska. Electronic Transport Properties of Carbon-Nanotube Networks: The Effect of Nitrate Doping on Intratube and Intertube Conductances. *Physical Review Applied*, 9, 034010, March 2018.

List of Publications

Author's Contribution

Publication I: “Enhancing conductivity of carbon nanotube networks by transition metal adsorption”

The author contributed to planning the project, searched for the relevant literature, performed all the calculations, and was the main author of the manuscript.

Publication II: “Conductivity of AuCl₄-Functionalized Carbon Nanotube Networks”

The author searched for previous articles related to the research topic, performed all the calculations, and was the main author of the manuscript.

Publication III: “Electronic Transport Properties of Carbon-Nanotube Networks: The Effect of Nitrate Doping on Intratube and Intertube Conductances”

The author participated in planning the project, carried out the calculations, and wrote the first version of the manuscript.

Author's Contribution

1. Introduction

Carbon is an interesting element that can form several different structures. One of these structures is a carbon nanotube (CNT). It is expected that CNTs can be used in the next-generation electronic devices [1]. In particular, CNT networks, systems comprising a large number of randomly oriented CNTs, could be used as transparent electrodes in several applications [2]. The applications include, for example, touch screens [3], solar cells [4], organic light-emitting diodes [5], and motion sensors [6].

The interest in CNT networks has increased because these materials can conduct electricity and are also transparent. Furthermore, the CNT networks are flexible and stretchable. However, the conductivity of the present CNT thin films should still be improved before they can be used in real applications. Previous experimental studies have shown a significant increase in the conductivity when group 6 transition metal atoms are deposited on the CNT thin films [7]. An essential topic of this work is examining the effect of these transition metal (TM) atoms that are Cr, Mo, and W on the conductances of CNT junctions. The CNT junctions account for most of the total sheet resistivity and should therefore be studied in more detail.

Tailoring the properties of CNT junctions can also be performed with molecular linkers [8] or with chemical functionalisation [9, 10]. For instance, doping of CNTs with metal iodides [11] or acids [12] results in an enhancement of the sheet conductivity. The second topic considered in this work is the doping of single-wall CNTs with AuCl_4 and NO_3 molecules, which describes the effect of AuCl_3 and nitric acid on the CNT network. Both individual doped CNTs and junctions of doped CNTs are investigated.

The atomic structures and band structures of the CNT systems are studied using density functional theory (DFT) calculations that can be combined with the usual Green's function method when electron transport in the system is considered. To examine the doping of CNTs, the band structures of the doped systems are determined. Then, charge transfer between the CNTs and the molecules is computed. Electron transport through CNT junctions is investigated by computing electronic transmission functions for four-terminal systems where two perpendicular CNTs form junctions that are coupled to semi-infinite CNT

leads.

The AuCl_4 and NO_3 molecules are found to cause a p-type doping effect in semiconducting CNTs. The metallic CNTs also become p-doped when they have adsorbed NO_3 molecules. Furthermore, pinning of the Fermi level to flat molecular states and van Hove singularities is found in the case of both molecules. Doping of semiconducting CNTs seems to be easier than that of metallic CNT systems because the charge transfer and the downshift of the Fermi level are larger in CNTs if they are originally semiconducting. In addition, $\text{NO}_3\text{-H}_2\text{O}$ complexes result in higher doping efficiencies than NO_3 molecules without water and the doping efficiency per molecule does not depend on the molecular concentration. Computing electronic transmission functions for CNT junctions shows that the conductance of the CNT junction enhances remarkably when the CNTs are linked with a TM atom. The electron transport through the CNT junction also enhances when the CNTs are doped with AuCl_4 or NO_3 molecules even without a linking molecule between the CNTs. Due to the pinning of the Fermi level to a region with a high density of states, the molecular doping is expected to be stable. The nitrate molecules cause a larger increase in the conductance of the junction of semiconducting CNTs than what the corresponding increase in a junction of metallic CNTs is.

2. Basic ideas of density functional theory

Describing properties of materials and devices at the nanoscale is a challenging task. It is well known that the methods of classical physics fail when the size of the system studied approaches the size of a molecule or an atom. Therefore, the methods of quantum theory are needed in order to understand the behaviour of the matter at the nanoscale. This theory has been successfully applied to various problems in modern physics. For example, the structure of matter and its properties can be understood using the tools of quantum mechanics.

2.1 Schrödinger equation and the wavefunction

The standard problem in quantum mechanics is solving the Schrödinger equation that can be written as

$$\hat{H}\Psi(\{\mathbf{r}_i\}; t) = i\hbar \frac{d\Psi(\{\mathbf{r}_i\}; t)}{dt}, \quad (2.1)$$

where \hat{H} is the Hamiltonian operator and the wavefunction Ψ depends on both the coordinates \mathbf{r}_i of N particles and time t . It is often sufficient to study systems without the time dependence and time in Eq. (2.1) can be neglected. Then the Schrödinger equation can be expressed as

$$\hat{H}\Psi = E\Psi. \quad (2.2)$$

In this case, the symbol E is energy and denotes the eigenvalue of the time-independent equation.

Analytical solutions to Eq. (2.2) cannot usually be obtained. Hence, numerical approaches to solve the equation for the wavefunction are needed. However, numerical methods can be applied only if the number of particles is small enough. On the other hand, a notable benefit of the wavefunction method is that several physical and chemical properties of nanoscale systems or bulk materials can be investigated when the wavefunction of the system has been solved, for instance, by using suitable approximations. Examples of these properties are the atomic structures of bulk materials, the character of bonds between the atoms, thermal properties of the system, and the electronic conductivity.

2.2 Determining the electron density

The problems in solid-state physics often start by defining the Hamiltonian for the system of interest. The Hamiltonian of a solid material contains, besides the kinetic energies of electrons and nuclei, terms describing the interactions of nuclei with electrons inside the matter and with other electrons. In addition, the interaction of nuclei with themselves has to be included in the model. In this specific case, the Hamiltonian is of the form [13]

$$\hat{H} = -\frac{\hbar^2}{2m_e} \sum_i \nabla_i^2 - \sum_{i,I} \frac{Z_I e^2}{|\mathbf{r}_i - \mathbf{R}_I|} + \frac{1}{2} \sum_{i \neq j} \frac{e^2}{|\mathbf{r}_i - \mathbf{r}_j|} - \sum_I \frac{\hbar^2}{2M_I} \nabla_I^2 + \frac{1}{2} \sum_{I \neq J} \frac{Z_I Z_J e^2}{|\mathbf{R}_I - \mathbf{R}_J|}. \quad (2.3)$$

Electrons are denoted by lower case subscripts in Eq. (2.3), whereas the upper case subscripts are for the nuclei. The first term describes the kinetic energy of electrons. The potential energy due to the electron-nucleus interaction is represented by the second term. The third term comes from the electron-electron interactions. Finally, the last two terms describe the kinetic and interaction energies of the nuclei, respectively. It is possible to simplify the expression in Eq. (2.3) by examining the kinetic energy term of the nuclei. Because the inverse mass of the nuclei can be considered small, their kinetic energy can be neglected, leading to the Born-Oppenheimer approximation. This is also called the adiabatic approximation.

It is obvious that the large number of particles in realistic systems makes solving the eigenvalues of the Hamiltonian in Eq. (2.3) very challenging. Therefore, this way of studying the properties of, e.g., solids is not plausible. In the 1960's, Hohenberg, Kohn, and Sham developed a new approach that is still used in today's studies of solid-state systems [14, 15]. The essential idea of the DFT is to write all physical quantities as functionals of the electron density $n(\mathbf{r})$. In the original work carried out by Hohenberg and Kohn, it is shown that the external potential for a system of interacting particles is determined uniquely, except for a constant, by the ground state density. As a result, finding the ground state density makes it possible to determine all physical properties of the system. Furthermore, minimising the energy functional $E[n]$ gives the ground state energy and the minimum is obtained with the exact ground state density.

The DFT is formulated as an exact theory and has been developed further in the past decades. However, practical calculations require an approximation for the interactions. A central idea of the Kohn-Sham DFT is to consider an independent-particle problem and express all the many-body effects using an exchange-correlation functional. If the exchange-correlation functional can be approximated well, the ground state density of the original many-body-problem is obtained by solving the independent-particle problem. For the actual calculations, the ground state energy functional for the system with all the

many-body interactions can be written as

$$E_{\text{KS}} = T_s[n] + \int d^3r V_{\text{ext}}(\mathbf{r})n(\mathbf{r}) + E_{\text{Hartree}}[n] + E_{II} + E_{\text{xc}}[n]. \quad (2.4)$$

The kinetic energy of the non-interacting system with N particles is represented by the term $T_s[n]$ in Eq. (2.4). In the second term in Eq. (2.4), V_{ext} describes the external potential coming from the nuclei and other external fields. In the same equation, the Coulomb interaction of the electron gas with itself is described by the Hartree energy E_{Hartree} and the term E_{II} is an interaction term for the nuclei shown in Eq. (2.3). Finally, the functional $E_{\text{xc}}[n]$ includes all the challenging many-body interactions.

Solving the independent-particle problem is possible by minimising the Kohn-Sham energy functional, which can be performed by varying the wavefunctions in Eq. (2.4). However, the energy functional depends on the density $n(\mathbf{r})$ that can be expressed as

$$n(\mathbf{r}) = \sum_{\sigma} \sum_{i=1}^{N^{\sigma}} |\psi_i^{\sigma}(\mathbf{r})|^2. \quad (2.5)$$

This relation is needed before the variational equation can be calculated because the electron density n has to be expressed in terms of the wavefunctions. In Eq. (2.5), spin is denoted by σ and ψ_i^{σ} is the wavefunction of the i th orbital with spin σ . The number of occupied orbitals is N^{σ} for each spin σ . Moreover, the constraint for the normalisation and the orthogonality has to be taken into account. Using the Lagrange multiplier method, it is possible to derive so-called Kohn-Sham equations [13]

$$(H_{\text{KS}}^{\sigma} - \epsilon_i^{\sigma})\psi_i^{\sigma}(\mathbf{r}) = 0, \quad (2.6)$$

where the ϵ_i^{σ} denote the eigenvalues, and the effective Hamiltonian can be written as

$$H_{\text{KS}}^{\sigma}(\mathbf{r}) = -\frac{1}{2}\nabla^2 + V_{\text{KS}}^{\sigma}(\mathbf{r}). \quad (2.7)$$

The effective Hamiltonian $V_{\text{KS}}^{\sigma}(\mathbf{r})$ contains an effective potential that is given by

$$\begin{aligned} V_{\text{KS}}^{\sigma}(\mathbf{r}) &= V_{\text{ext}}(\mathbf{r}) + \frac{\delta E_{\text{Hartree}}(\mathbf{r})}{\delta n(\mathbf{r}, \sigma)} + \frac{\delta E_{\text{xc}}(\mathbf{r})}{\delta n(\mathbf{r}, \sigma)} \\ &= V_{\text{ext}}(\mathbf{r}) + V_{\text{Hartree}}(\mathbf{r}) + V_{\text{xc}}^{\sigma}(\mathbf{r}). \end{aligned} \quad (2.8)$$

The exchange-correlation potential V_{xc} can have different forms because a significant number of different exchange-correlation functionals have been developed. Equations (2.6)-(2.8) have been written using the Hartree units.

2.3 Exchange-correlation functionals

A very important feature of the Kohn-Sham DFT is that the total energy functional can be divided into kinetic, potential, and exchange-correlation energy

terms. Furthermore, the exchange-correlation energy E_{xc} can often be approximated as a local or nearly local functional of the density [13]. Thus, the energy E_{xc} is of the form

$$E_{xc}[n] = \int d^3r n(\mathbf{r}) \epsilon_{xc}([n], \mathbf{r}), \quad (2.9)$$

where $\epsilon_{xc}([n], \mathbf{r})$ is the energy density, an energy per electron at point \mathbf{r} . The energy density depends only on the electron density within a small region close to the point \mathbf{r} . This kind of a formula for the exchange-correlation energy E_{xc} is simple but works quite well because, e.g., solids can often be regarded as homogeneous electron gases where the character of exchange-correlation effects is local. The local density approximation (LDA) and its extension, the local spin density approximation (LSDA) allow us to compute E_{xc} in a straightforward way. The exchange-correlation energy for the LSDA can be written as

$$\begin{aligned} E_{xc}^{\text{LSDA}}[n^\uparrow, n^\downarrow] &= \int d^3r n(\mathbf{r}) \epsilon_{xc}^{\text{hom}}(n^\uparrow(\mathbf{r}), n^\downarrow(\mathbf{r})) \\ &= \int d^3r n(\mathbf{r}) [\epsilon_x^{\text{hom}}(n^\uparrow(\mathbf{r}), n^\downarrow(\mathbf{r})) + \epsilon_c^{\text{hom}}(n^\uparrow(\mathbf{r}), n^\downarrow(\mathbf{r}))]. \end{aligned} \quad (2.10)$$

In Eq. (2.10), $n(\mathbf{r})$ is the total electron density and $\epsilon_{xc}^{\text{hom}}(n^\uparrow(\mathbf{r}), n^\downarrow(\mathbf{r}))$ describes the exchange-correlation energy density of the homogeneous electron gas. The terms $n^\uparrow(\mathbf{r})$ and $n^\downarrow(\mathbf{r})$ are the electron densities of the up and down spins, respectively. The exchange-correlation term $\epsilon_{xc}^{\text{hom}}$ can be written as a sum of the exchange energy density ϵ_x^{hom} and the correlation energy density ϵ_c^{hom} of the homogeneous electron gas.

The assumption of a homogeneous electron gas in the LDA is known to work even in some inhomogeneous cases. However, the simplicity of the approximation can decrease the accuracy of DFT calculations. To improve the accuracy, the gradient of the density can be included in the exchange-correlation energy in Eq. (2.9). This method, however, does not lead to remarkably more accurate calculations because the density gradients in real materials are so large that the gradient expansion is not valid and significant modulations appear in the exchange potential [16]. Instead, better results are obtained when gradients of higher order are also taken into account. In the generalised-gradient approximation (GGA), the exchange-correlation functional becomes

$$\begin{aligned} E_{xc}^{\text{GGA}}[n^\uparrow, n^\downarrow] &= \int d^3r n(\mathbf{r}) \epsilon_{xc}(n^\uparrow, n^\downarrow, |\nabla n^\uparrow|, |\nabla n^\downarrow|, \dots) \\ &= \int d^3r n(\mathbf{r}) \epsilon_x^{\text{hom}}(n) F_{xc}(n^\uparrow, n^\downarrow, |\nabla n^\uparrow|, |\nabla n^\downarrow|, \dots), \end{aligned} \quad (2.11)$$

where $\epsilon_x^{\text{hom}}(n)$ denotes the exchange energy of the homogeneous electron gas without spin polarisation and $F_{xc}(n^\uparrow, n^\downarrow, |\nabla n^\uparrow|, |\nabla n^\downarrow|, \dots)$ is the exchange-correlation enhancement factor.

Practical calculations require parametrised analytic functions for the exchange energy ϵ_x^{hom} and the exchange-correlation enhancement factor F_{xc} . An example

of the GGA functionals is the Perdew-Wang 1991 (PW91) functional [17]. This functional has been constructed so that certain exact conditions are satisfied.

One of the most popular GGA functionals is the Perdew-Burke-Ernzerhof (PBE) functional [18]. This functional attempts to solve the problems associated with PW91. One drawback of the PW91 functional is that the analytic function fitted to the numerical results is complicated and overparametrised. In addition, the parameters of the function are not seamlessly joined. As a result, some variations appear in the exchange-correlation potential for small and large density gradients. An additional problem is that PW91 reduces to the second-order gradient expansion for slowly varying or small density variations and therefore the linear response of the density of a homogeneous electron gas cannot be described as well as with the LSDA. The linear response behaviour is important, e.g., in the pseudopotential theory of metals.

The correlation energy of the PBE functional is of the form

$$E_C^{\text{PBE}}[n_\uparrow, n_\downarrow] = \int d^3r n [e_C^{\text{hom}}(r_s, \zeta) + H(r_s, \zeta, t)], \quad (2.12)$$

where r_s is the local Seitz radius, $\zeta = (n_\uparrow - n_\downarrow)/n$ is the relative spin polarisation, and $t = |\nabla n|/(2\phi k_s n)$ is a dimensionless density gradient. In Eq. (2.12), e_C^{hom} denotes the correlation energy of a homogeneous electron gas. The spin-scaling factor is defined by the function $\phi(\zeta) = [(1 + \zeta)^{2/3} + (1 - \zeta)^{2/3}]/2$, and $k_s = \sqrt{4k_F/(\pi a_0)}$, where $a_0 = \hbar^2/(me^2)$, is the Thomas-Fermi screening wave number. The local Seitz radius r_s describes the average distance between the electrons in a homogeneous electron gas and is related to the electron density $n = 3/(4\pi r_s^3) = k_F^3/(3\pi^2)$. The Fermi wavevector is denoted by k_F in the previous expressions. The gradient term H in Eq. (2.12) is based on a few requirements. The first requirement is that H is given by its second-order gradient expansion in the slowly varying limit when $t \rightarrow 0$. According to the second condition, the gradient correction $H \rightarrow -e_C^{\text{hom}}$ as $t \rightarrow \infty$. The third requirement for the H term is that the correlation energy E_C has to scale to a constant under uniform scaling of the density. All these three conditions can be satisfied by choosing an appropriate form for the H term that is shown in Ref. [18]. Testing the scaling behaviour with a two-electron ion having a nuclear charge $Z \rightarrow \infty$ gives a correlation energy that is quite close to the exact value.

The exchange energy part of the PBE functional can be constructed considering a few extra requirements. A proper exchange energy should also satisfy a scaling condition similarly to that for the correlation part. This condition specifies the form of the exchange energy that is given by [18]

$$E_X^{\text{PBE}} = \int d^3r n e_X^{\text{hom}}(n) F_X(s). \quad (2.13)$$

In Eq. (2.13), the exchange energy of the homogeneous electron gas is $e_X^{\text{hom}} = -3e^2 k_F/(4\pi)$. Another condition is that the exchange energy should obey the spin-scaling relationship. Furthermore, the linear response of the homogeneous electron gas is required and fulfilling the condition for the Lieb-Oxford bound is

also needed. These requirements together lead to the exchange enhancement factor

$$F_X(s) = 1 + \kappa - \kappa/(1 + \mu s^2/\kappa), \quad (2.14)$$

where μ and κ are parameters. The expression (2.14) is the last term in Eq. (2.13). Finally, one can define the total enhancement factor F_{XC} over the local exchange using the exchange-correlation energy

$$E_{XC}^{\text{PBE}}[n_\uparrow, n_\downarrow] = \int d^3r n c_X^{\text{hom}}(n) F_{XC}(r_s, \zeta, s). \quad (2.15)$$

A remarkable benefit of the PBE exchange-correlation functional is that all parameters in the functional excluding those of the LSDA are fundamental constants. The PBE functional also includes several other advantages the most important of which are a precise description of the linear response of the homogeneous electron gas, correct behaviour under the uniform scaling of the electron gas, and also a smoother potential.

2.4 Hybrid exchange-correlation functionals

Semilocal functionals are commonly used in DFT to model exchange-correlation effects. However, the semilocal functionals including the PBE functional have several shortcomings. They usually underestimate the band gaps of materials [19]. This problem occurs both in the case of LDA and GGA functionals. Actually, adding the gradient part to the functional does not improve the accuracy of the functional so much. To obtain more realistic and precise band gap values, new kinds of exchange-correlation functionals have been developed. Examples of these functionals are hybrid density functionals that include a portion of Hartree-Fock exchange. This improves the accuracy of the functional but also makes the computations heavier than those performed with semilocal functionals.

In recent years, the Heyd-Scuseria-Ernzerhof (HSE) hybrid functional has become popular among other modern functionals [20, 21]. The latest version of this functional is called HSE06 because its improved and corrected version was introduced in 2006. Computing the exact exchange is challenging for metallic systems since the $1/r$ Coulomb potential has a singularity. To make calculations converge faster, a screened Coulomb potential can be used. In the case of the HSE06 functional, the Coulomb operator is split into short-range and long-range components and the final expression is [20]

$$\frac{1}{r} = \frac{\text{erfc}(\omega r)}{r} + \frac{\text{erf}(\omega r)}{r}. \quad (2.16)$$

In Eq. (2.16), ω is an adjustable parameter and $\text{erfc}(\omega r) = 1 - \text{erf}(\omega r)$. The first term $\text{erfc}(\omega r)/r$ denotes the short-range part. Correspondingly, the second term $\text{erf}(\omega r)/r$ describes the long-range part. The form of the exchange-correlation energy of the HSE06 hybrid functional originates from the PBE0 hybrid functional

[22]. The total exchange-correlation energy of the PBE0 is

$$E_{xc}^{\text{PBE0}} = aE_x^{\text{HF}} + (1-a)E_x^{\text{PBE}} + E_c^{\text{PBE}}, \quad (2.17)$$

where the mixing coefficient is $a = 1/4$, E_x is the exchange energy, and E_c denotes the correlation energy. The value of the mixing coefficient can be derived using perturbation theory. The first two terms in Eq. (2.17) form the exchange part which can be divided into short- and long-range components. Then the exchange energy can be expressed as

$$E_x^{\text{PBE0}} = aE_x^{\text{HF,SR}}(\omega) + aE_x^{\text{HF,LR}}(\omega) + (1-a)E_x^{\text{PBE,SR}}(\omega) + E_x^{\text{PBE,LR}}(\omega) - aE_x^{\text{PBE,LR}}(\omega). \quad (2.18)$$

Computational studies have shown that the long-range parts of the PBE and HSE06 functionals cancel each other when the screening parameter ω is set to a realistic value. As a result, the hybrid density functional with a screened Coulomb potential becomes

$$E_{xc}^{\omega\text{PBEh}} = aE_x^{\text{HF,SR}}(\omega) + (1-a)E_x^{\text{PBE,SR}}(\omega) + E_x^{\text{PBE,LR}}(\omega) + E_c^{\text{PBE}}. \quad (2.19)$$

The exchange-correlation energy in Eq. (2.19) has a tunable parameter ω that determines the extent of the short-range interactions. In the case of the HSE06 functional [21], the screening parameter is set to $\omega = 0.11 \text{ bohr}^{-1} \approx 0.2 \text{ \AA}^{-1}$. Setting the screening parameter in Eq. (2.19) to $\omega = 0$ leads to the exchange-correlation energy of the PBE0 hybrid functional. Moreover, the expression in Eq. (2.19) is asymptotically similar to the PBE functional when $\omega \rightarrow \infty$. The calculations of the exchange energy terms are presented in Ref. [20].

2.5 Including the van der Waals correction and overview of the FHI-aims code package

Describing van der Waals interactions has turned out to be a considerable challenge in DFT. The van der Waals interactions originate from electron density fluctuations in materials and are important, for instance, in the structures of DNA, proteins, and other biochemical systems. Moreover, molecules on surfaces are also examples of systems where van der Waals interactions should be taken into account. Calculating potential energy curves for rare gas diatomic molecules has shown that conventional DFT calculations do not give good results [23]. The potential energy curve computed with LDA always has a minimum. However, the LDA calculations overestimate the dissociation energies of the molecules. Performing the same DFT calculations with a GGA functional results in repulsive potential energy curves. Therefore, a standard GGA functional cannot describe the van der Waals interaction so well. Replacing part of the exchange with exact exchange enhances the binding but underestimates the dissociation energies. In this case, the binding can still be regarded as weak.

Thus, DFT without any modifications is not able to describe the dispersion or van der Waals interactions properly [24].

Correcting the error of van der Waals interactions in DFT calculations is possible by modifying the exchange-correlation energy term that is given by [25]

$$E_{xc} = \int d^3r_1 \int d^3r_2 K_{xc}(\mathbf{r}_1, \mathbf{r}_2) \delta n(\mathbf{r}_1) \delta n(\mathbf{r}_2), \quad (2.20)$$

where the linear response kernel K_{xc} represents the exchange-correlation energy of a slightly non-uniform system and δn is the deviation in charge density with respect to the uniform system. Approximating the effective density is necessary in order to meet the requirements for the uniform gas and separate limits. As shown in Ref. [25], promising expressions for the effective long-range electron interactions are obtained when the effective electron density is written as

$$n_{\text{eff}} = \left[\sqrt{n(\mathbf{r}_1)n(\mathbf{r}_2)} \left(\sqrt{n(\mathbf{r}_1)} + \sqrt{n(\mathbf{r}_2)} \right) \right]^{2/3}. \quad (2.21)$$

Then it is possible to construct a formula for the electron interaction that can be integrated to derive an expression for the long-range part of the exchange-correlation energy. It is given by

$$E_{xc}^{l-r} = -\frac{3}{\pi} \int_0^\infty du \int_{V_1} d^3r_1 \int_{V_2} d^3r_2 \frac{\chi_1(iu)\chi_2(iu)}{|\mathbf{r}_1 - \mathbf{r}_2|^6}, \quad (2.22)$$

where $\chi(iu)$ is the electric susceptibility. If two atoms are separated by a distance R , Eq. (2.22) can be expressed as

$$E_{xc}^{l-r} = -\frac{C_6}{R^6}, \quad (2.23)$$

where the van der Waals constant C_6 can be written as

$$C_6 = \frac{3}{\pi} \int_0^\infty du \alpha_1(iu)\alpha_2(iu), \quad (2.24)$$

and the atomic polarisability α_i is given by

$$\alpha_i(\omega) = \int d^3r \chi_i(\omega). \quad (2.25)$$

The integral in the expression for the polarisability in Eq. (2.25) is calculated over the volume of the atom. The idea of modifying the exchange-correlation energy term according to Ref. [25] has been implemented in several different DFT code packages and the functional is often called the LL functional according to its developers Langreth and Lundqvist. A benefit of the LL functional is that it is completely non-empirical and has the correct decay behaviour as a function of the separation R [24].

Another quite a promising way of taking the van der Waals correction into account in DFT calculations is to develop an empirical correction scheme that includes several parameters which come from a fitting procedure. A functional called B97-D proposed by Grimme has turned out to be accurate [26]. This

method is based on Becke's GGA functional, where the gradient corrections are expanded in power series. The total energy is defined as [26]

$$E = E_{\text{KS-DFT}} + E_{\text{disp}}, \quad (2.26)$$

where $E_{\text{KS-DFT}}$ is the self-consistent Kohn-Sham energy of the DFT calculation and E_{disp} denotes an empirical correction term. The correction term can be expressed as

$$E_{\text{disp}} = -s_6 \sum_{i=1}^{N_{\text{at}}-1} \sum_{j=i+1}^{N_{\text{at}}} \frac{C_6^{ij}}{R_{ij}^6} f_{\text{dmp}}(R_{ij}). \quad (2.27)$$

In Eq. (2.27), N_{at} is the number of atoms in the system, C_6^{ij} is the dispersion coefficient for an atom pair ij , s_6 is a global scaling factor, and R_{ij} is an interatomic distance. Furthermore, a damping factor $f_{\text{dmp}}(R_{ij})$ is needed to avoid singularities for small R . The damping function is given by

$$f_{\text{dmp}}(R_{ij}) = \frac{1}{1 + e^{-d(R_{ij}/R_r - 1)}}, \quad (2.28)$$

where R_r is the sum of atomic van der Waals radii and d is a parameter.

The performance of the B97-D functional is good compared with other widely used functionals [26]. For instance, heats of formation computed with B97-D for the G2/97 standard test set with 148 entries are more accurate than the same quantities calculated with GGA functionals PBE and BLYP. Even the meta-GGA functional TPSS leads to a larger mean absolute deviation from experimental reference values of the heats of formation than the B97-D functional. Its error is almost as small as that of the B3LYP hybrid functional. Other tests regarding chemical reactions and transition metal complexes have shown that B97-D usually gives more precise reaction energies than those computed with other functionals. Moreover, the deviations of the atomisation energies from the reference values are significantly smaller when calculations for group II clusters with Be, Mg, and Ca atoms are carried out with the B97-D functional instead of TPSS or B3LYP.

The interatomic $C_6 R^{-6}$ terms make it possible to include the van der Waals correction in DFT calculations but a remarkable problem with these terms is often that they are determined empirically. The accuracy and reliability of the $C_6 R^{-6}$ correction scheme can be improved by determining the C_6 coefficients from the mean-field ground-state electron density and precise reference data for free atoms as has been shown by Tkatchenko and Scheffler [27]. The expression for the C_6 coefficient in Eq. (2.24) can be used to calculate a new term C_6^{ij} describing the van der Waals interaction between two atoms or molecules 1 and 2. In the method presented in Ref. [27], the atomic polarisability of the first atom is of the form

$$\alpha_i^1(\omega) = \frac{\alpha_i^0}{1 - (\omega/\eta_i)^2}, \quad (2.29)$$

where α_i^0 is the static polarisability and η_i is an effective frequency. When the atomic polarisability α_i in Eq. (2.24) is replaced by the expression shown in

Eq. (2.29), the van der Waals coefficient becomes

$$C_6^{ij} = \frac{3}{2}[\eta_i\eta_j/(\eta_i + \eta_j)]\alpha_i^0\alpha_j^0. \quad (2.30)$$

If both atoms are identical ($i = j$), the effective frequency can be written as

$$\eta_i = \frac{4}{3} \frac{C_6^{ii}}{(\alpha_i^0)^2}. \quad (2.31)$$

The formula in Eq. (2.31) together with Eq. (2.30) leads to a new expression for the C_6^{ij} coefficient. It is given by

$$C_6^{ij} = \frac{2C_6^{ii}C_6^{jj}}{\frac{\alpha_j^0}{\alpha_i^0}C_6^{ii} + \frac{\alpha_i^0}{\alpha_j^0}C_6^{jj}}. \quad (2.32)$$

Computing the C_6^{ij} coefficient requires the free-atom reference values α_i^0 and C_6^{ii} and they can be found in literature. In Ref. [27], the C_6 coefficient is also defined for an atom inside a molecule or a solid and is called an effective coefficient $C_{6,\text{eff}}^{ij}$. The main ideas of the method are described in Ref. [27] in more detail. When the van der Waals coefficients C_6^{ij} are known, an intermolecular coefficient C_6^{mol} can be calculated as a sum

$$C_6^{\text{mol}} = \sum_i \sum_j C_{6,\text{eff}}^{ij}, \quad (2.33)$$

where the indices i and j refer to the atoms in the first and second molecule, respectively. An extensive test study of 1225 intermolecular pairs in Ref. [27] shows that the mean absolute relative error of the test data is small compared with other existing methods. Furthermore, the error does not depend significantly on the three functionals (LDA, PBE, and BLYP) used in the calculations.

Practical DFT calculations are often carried out using some code package. In this work, we have mainly used the FHI-aims code package [28]. It is an all-electron full-potential DFT code and is based on numerical atom-centred orbitals. Actually, the orbitals of the FHI-aims code also contain an analytically defined part. A remarkable benefit of these numerical atom-centred orbitals used in the FHI-aims code is that the spatial regions of large systems do not interact with each other. Thus, the calculations scale nearly linearly with the number of atoms in the system. The numerical atomic orbitals can also be used to construct molecular orbitals [29]. A marked task in the DFT calculations is performing the integrations using appropriate grids. In Ref. [30], various top-down methods to generate integration grids are presented. The grid points play an important role in the efficiency of the code because the scaling is linear only when a suitable grid is chosen for the calculations.

3. Computing transmission functions

3.1 Conductance of a nanoscale device

The conductivity of nanoscale devices is a rather complex issue and studying such devices requires methods developed particularly for describing the electrical conductivity of systems where the nanoscale effects are important. A well-known method for calculating the conductance of a nanoscale system is the Landauer-Büttiker formalism. According to this formalism, the conductance G of the system can be written as [31]

$$G = \frac{2e^2}{h}MT \quad (3.1)$$

where M is the number of propagating modes and T denotes the average probability that an electron can go through the conductor. The expression in Eq. (3.1) has been written in the form where the dependence of the number of modes M and of the probability T on energy is neglected. In a more complex system, both M and T are functions of the energy E .

The current through the nanoscale conductor can be computed by applying Eq. (3.1). If the transport occurs through multiple energy channels, then the current through each channel is [31]

$$\begin{aligned} i(E) &= \frac{2e}{h} [M(E)T(E)f_1(E) - M'(E)T'(E)f_2(E)] \\ &= \frac{2e}{h} [\bar{T}(E)f_1(E) - \bar{T}'(E)f_2(E)] \\ &= \frac{2e}{h} \bar{T}(E)[f_1(E) - f_2(E)] \end{aligned} \quad (3.2)$$

The functions f_1 and f_2 represent the energy distributions of the electrons in the first and second lead, respectively. The quantities with primes ($M'(E)$ and $T'(E)$) denote the current flowing in the opposite direction. The formula for the current can be simplified if we assume that $\bar{T}(E) = \bar{T}'(E)$. The quantity $\bar{T}(E)$ includes information about the number of modes M and can be regarded as an average transmission probability.

The total current is obtained by integrating the current formula (Eq. (3.2)) and is given by

$$I = \int i(E)dE. \quad (3.3)$$

In the linear response regime, the conductance of the system can be written as

$$G = \frac{2e^2}{h} \int \bar{T}(E) \left(-\frac{\partial f_0}{\partial E} \right) dE. \quad (3.4)$$

The function f_0 is the equilibrium Fermi function in Eq. (3.4). In the case of zero temperature, the partial derivative in the previous formula becomes a delta function and the conductance in the linear response regime can be expressed simply as

$$G = \frac{2e^2}{h} T(E_F). \quad (3.5)$$

3.2 Transport system

The Landauer formula in Eq. (3.1) enables calculating the conductance of the system if the quantities M and T are known. In particular, the objective of our work is to study the electrical conductivity of various CNT systems by evaluating electronic transmission functions for them. In the context of electron transport calculations, the transmission function T can be computed by determining the Green's function for the system investigated. An example of a transport system comprising a conductor and two semi-infinite leads is presented in Fig. 3.1.

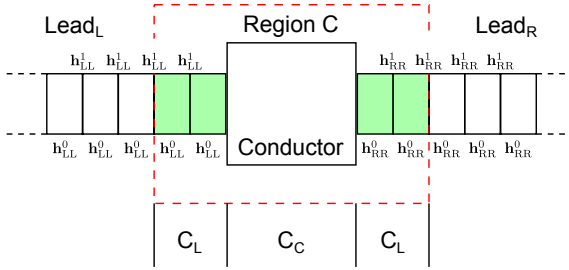


Figure 3.1. A two-terminal transport system. The conductor is connected to two semi-infinite leads that are denoted by Lead_L and Lead_R. The centre part called Region C can be divided into parts C_C and C_L that are the actual conductor and the ends of the leads (marked with light green colour), respectively. Moreover, the leads consist of principal layers shown by vertical rectangles. The Hamiltonian matrices within the principal layers are denoted by h_{LL}^0 (h_{RR}^0) for the left (right) lead. Correspondingly, the Hamiltonian matrices between two neighbouring principal layers are h_{LL}^1 and h_{RR}^1 .

The electron transport through the device displayed in Fig. 3.1 can be understood if the whole system is divided into small parts. This kind of partitioning is useful and makes it possible to construct, for instance, the Hamiltonians for

the semi-infinite leads and the centre region. The total Hamiltonian \hat{H} of the transport system can be expressed as

$$\hat{H} = \hat{H}_{LL} + \hat{H}_{CC} + \hat{H}_{RR} + \hat{H}_{LC} + \hat{H}_{CR}, \quad (3.6)$$

where \hat{H}_{LL} , \hat{H}_{CC} , and \hat{H}_{RR} are the Hamiltonians of the left lead, the Region C, and the right lead. The left and right leads are in Fig. 3.1 the Lead_L and Lead_R , respectively. Moreover, the last terms \hat{H}_{LC} and \hat{H}_{CR} are the Hamiltonians between the leads and the centre part, Region C.

Computing the Green's function for the transport system requires that the Hamiltonian in Eq. 3.6 is expanded in some appropriate basis set. A localised basis set is a good choice. With this basis set, the interaction Hamiltonian matrices \mathbf{H}_{LC} and \mathbf{H}_{CR} become finite. Furthermore, only interactions between the principal layer and its two nearest neighbors are considered meaning that the lead matrices \mathbf{H}_{LL} and \mathbf{H}_{RR} have block tridiagonal structures. Then the matrix \mathbf{H}_{LL} , for instance, can be expressed as

$$(\mathbf{H}_{LL})_{ij} = \begin{cases} \mathbf{h}_{LL}^0 & \text{if } i - j = 0, \\ \mathbf{h}_{LL}^1 & \text{if } i - j = 1, \\ (\mathbf{h}_{LL}^1)^\dagger & \text{if } j - i = 1, \\ 0 & \text{if } |i - j| > 1. \end{cases} \quad (3.7)$$

The matrices \mathbf{h}_{LL}^0 and \mathbf{h}_{LL}^1 are the Hamiltonian matrices within and between the principal layers, respectively. The meaning of these matrices is explained in the caption of Fig. 3.1. The matrix of the right lead can be written in a similar form. In addition, the non-zero parts of the matrices \mathbf{H}_{LC} and \mathbf{H}_{CR} are \mathbf{h}_{LL}^1 and \mathbf{h}_{RR}^1 , respectively.

We can calculate the matrix Green's function \mathbf{G} for the transport system by solving the equation

$$(\mathbf{E}\mathbf{S} - \mathbf{H})\mathbf{G}(E) = \mathbf{I}. \quad (3.8)$$

The first term before the equality sign in Eq. (3.8) can also be written as

$$\begin{pmatrix} \mathbf{E}\mathbf{S}_{LL} - \mathbf{H}_{LL} & \mathbf{E}\mathbf{S}_{LC} - \mathbf{H}_{LC} & 0 \\ \mathbf{E}\mathbf{S}_{LC}^\dagger - \mathbf{H}_{LC}^\dagger & \mathbf{E}\mathbf{S}_{CC} - \mathbf{H}_{CC} & \mathbf{E}\mathbf{S}_{CR} - \mathbf{H}_{CR} \\ 0 & \mathbf{E}\mathbf{S}_{CR}^\dagger - \mathbf{H}_{CR}^\dagger & \mathbf{E}\mathbf{S}_{RR} - \mathbf{H}_{RR} \end{pmatrix} \begin{pmatrix} \mathbf{G}_{LL} & \mathbf{G}_{LC} & \mathbf{G}_{LR} \\ \mathbf{G}_{CL} & \mathbf{G}_{CC} & \mathbf{G}_{CR} \\ \mathbf{G}_{RL} & \mathbf{G}_{RC} & \mathbf{G}_{RR} \end{pmatrix} \quad (3.9)$$

and the identity matrix \mathbf{I} is

$$\begin{pmatrix} \mathbf{I}_{LL} & 0 & 0 \\ 0 & \mathbf{I}_{CC} & 0 \\ 0 & 0 & \mathbf{I}_{RR} \end{pmatrix}. \quad (3.10)$$

Furthermore, \mathbf{S} is the overlap matrix. It is essential to solve Eq. (3.8) for the Green's function G_{CC} corresponding to Region C of the transport system. To

calculate G_{CC} , the element (2,2) of the matrix (3.9) has to be considered. Then, we can write a new expression for the Green's function in the form

$$(E\mathbf{S}_{LC}^\dagger - \mathbf{H}_{LC}^\dagger)\mathbf{G}_{LC} + (E\mathbf{S}_{CC} - \mathbf{H}_{CC})\mathbf{G}_{CC} + (E\mathbf{S}_{CR} - \mathbf{H}_{CR})\mathbf{G}_{RC} = \mathbf{I}_{CC} \quad (3.11)$$

In addition, the formulas for the Green's functions \mathbf{G}_{LC} and \mathbf{G}_{RC} are required before \mathbf{G}_{CC} can be computed. We can express \mathbf{G}_{LC} in the form

$$\mathbf{G}_{LC} = -(E\mathbf{S}_{LL} - \mathbf{H}_{LL})^{-1}(E\mathbf{S}_{LC} - \mathbf{H}_{LC})\mathbf{G}_{CC}. \quad (3.12)$$

The formula in Eq. (3.12) comes from the matrix element (1,1) in Eq. (3.9) and a similar expression for \mathbf{G}_{RC} can be determined. By combining Eqs. (3.11) and (3.12), a new equation for the Green's function \mathbf{G}_{CC} can be written if \mathbf{G}_{RC} is also expressed as a function of \mathbf{G}_{CC} . This equation is given by

$$\mathbf{G}_{CC} = (E\mathbf{S}_{CC} - (\mathbf{H}_{CC} + \Sigma_L(E) + \Sigma_R(E)))^{-1}, \quad (3.13)$$

where Σ_L and Σ_R are self-energies of the left and right semi-infinite leads, respectively. The expression for the left self-energy is

$$\Sigma_L(E) = (E\mathbf{S}_{LC} - \mathbf{H}_{LC})^\dagger G_{LL}^0(E)(E\mathbf{S}_{LC} - \mathbf{H}_{LC}) \quad (3.14)$$

and $G_{LL}^0(E)$ in Eq. (3.14) is the retarded Green's function of the left semi-infinite lead. By replacing the sub- or superscript index L with R in the formula (3.14), a corresponding expression for the right self-energy can be calculated. The retarded Green's function $G_{LL}^0(E)$ can be written as

$$G_{LL}^0(E) = (z\mathbf{S}_{LL} - \mathbf{H}_{LL})^{-1}, \quad (3.15)$$

where the quantity z is given by $z = E + i\eta$ and η is a small broadening parameter.

Computing the self-energies for the semi-infinite leads can be performed using the localised basis set in quite a simple manner. For instance, the left self-energy becomes

$$\Sigma_L(E) = (E\mathbf{s}_{LL}^1 - \mathbf{h}_{LL}^1)^\dagger \mathbf{g}_{LL}^0(E)(E\mathbf{s}_{LL}^1 - \mathbf{h}_{LL}^1), \quad (3.16)$$

where the lower-case overlap and Hamiltonian matrices are finite non-zero parts of the upper-case matrices. Furthermore, $\mathbf{g}_{LL}^0(E)$ is related to the 0th principal layer of the left lead. Correspondingly, the other Green's function $\mathbf{g}_{RR}^0(E)$ comes from the 0th principal layer of the right lead. One possibility to determine $\mathbf{g}_{LL}^0(E)$ is to use a block recursion method. In this method, the surface Green's function $\mathbf{g}_{LL}^0(E)$ is calculated using the expression

$$\mathbf{g}_{LL}^0(E) = [z\mathbf{s}_{LL}^0 - \mathbf{h}_{LL}^0 - (z\mathbf{s}_{LL}^1 - \mathbf{h}_{LL}^1)^\dagger \mathbf{g}_{LL}^0(E)(z\mathbf{s}_{LL}^1 - \mathbf{h}_{LL}^1)]^{-1}. \quad (3.17)$$

The quantity z in the previous equation has the same meaning as that of a similar symbol in Eq. (3.15). After computing the Green's function for the centre region, the transmission function can be calculated. The transmission function between the left and right leads can be written as

$$T_{L-R}(E) = \text{Tr}(\Gamma_L(E)G^r(E)\Gamma_R(E)G^a(E)), \quad (3.18)$$

where the expression for Γ_L is $\Gamma_L(E) = i(\Sigma_L^r(E) - \Sigma_L^a(E))$. The functions G^a and Σ^a are the Hermitian conjugates of G^r and Σ^r , respectively.

3.3 Numerical calculation of the transmission function

The electronic transmission functions for CNT systems are computed using the transport module of the FHI-aims code package. An electron transport calculation involves two steps. In the first step, a ground-state DFT calculation is carried out for the computational unit cells of the leads. The purpose of this calculation is to store the non-zero elements of the Hamiltonian and overlap matrices for the second step. The second step consists of a calculation where the self-energies for the leads are determined and the Green's function for the central region is computed.

The FHI-aims code computes the Green's function using the expression (3.17) and in this case the energy variable z is varied until the Green's function is close enough to the solution of the equation. To compute the Green's function for the leads, an initial guess for the function is needed. This guess can be computed by solving the Green's function for the expression $z\mathbf{S}_L^0 - \mathbf{H}_L^0$. Then, we can carry out the iteration. During the iteration, several matrix operations are needed and factorisation of the matrices is also required, which can be performed with the methods of the SCALAPACK library. The iteration is stopped when the numerically computed Green's function is close to the real solution. The convergence of the function is checked by comparing the Green's function matrices of two successive steps. A condition for stopping the iteration comes from the elements of the Green's functions matrices. When the largest absolute value of the Green's function matrix changes less than the tolerance, the iteration is stopped. Then, the self-energy for the lead can be computed. The steps of the lead calculation are presented in Fig. 3.2.

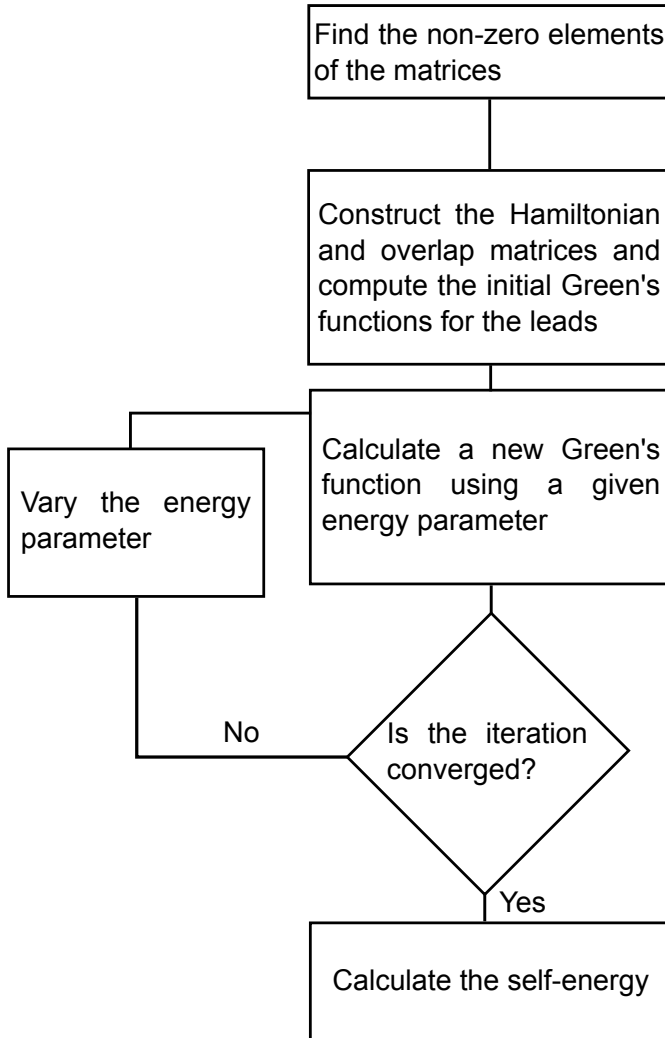


Figure 3.2. Flowchart of the self-energy calculation in the transport module of the FHI-aims code package.

After computing the self-energies for the leads, the Green's function for the central region \mathbf{G}_{CC} is calculated. The transport module of the FHI-aims code first constructs the Hamiltonian matrix of the form $E\mathbf{S} - \mathbf{H}$, from which the self-energies Σ_i^r are subtracted. Thereafter, \mathbf{G}_{CC} can be calculated using Eq. (3.13). Finally, the electronic transmission function as a function of energy is obtained by evaluating the trace of the matrix product according to Eq. (3.18). The algorithm of the transport calculation is shown in Fig. 3.3.

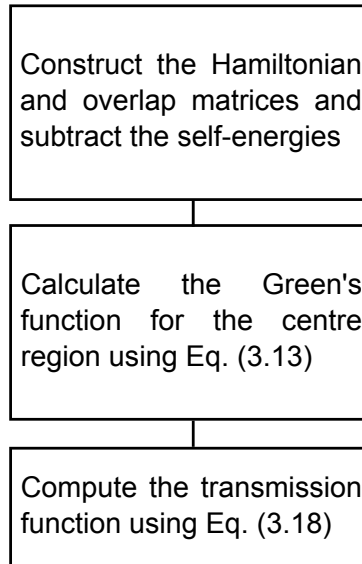


Figure 3.3. Flowchart of the calculation for the transmission function in the transport module of the FHI-aims code package.

Computing transmission functions

4. Carbon nanotube thin films

Numerous methods to fabricate CNT thin films have been developed. The synthesis methods can be divided into two categories that are dry and wet processes [32]. The dry processes often lead to high sheet conductivity whereas a benefit of the wet methods is the compatibility with some industrial fabrication processes. An example of the dry processes is floating catalyst chemical vapour deposition. With this method, high-quality CNT thin films have been obtained. The wet processes include, for instance, the dip-coating, spray coating, Langmuir-Blodgett technique, and vacuum filtration [32].

The CNT thin films are commonly used as transparent electrodes in applications [1, 32]. In particular, the CNT thin films could replace indium tin oxide (ITO) in several touch screen systems. The drawback of ITO is that indium is a scarce material. In addition, ITO systems cannot be bent so much as CNT thin films. Therefore, using CNT thin films in new kinds of flexible touch screens or displays may be possible if the electrical properties of the CNT thin films can be improved. A common challenge related to the CNT networks is fabricating thin films where the transparency is high and the resistivity is low simultaneously. The transmittance as a function of the resistivity can be seen in Fig. 4.1. A decrease in the resistivity also results in a rapid decrease in the transmittance. Thus, finding optimal sheet parameters can be challenging. However, the CNT thin films have been used in several applications including displays, touch screens, solar cells, light-emitting diodes, thin-film transistors, defrosting systems for windows, and electromagnetic shields [1].

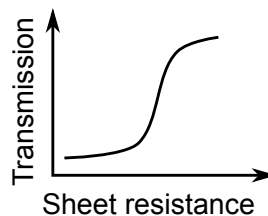


Figure 4.1. Schematic figure of the transmission of a CNT thin film as a function of the sheet resistance.

4.1 Conductivity of the carbon nanotube network

The electrical conductivity of a CNT network depends on the structure of the network (network morphology) as well as on the properties of individual CNTs and their junctions [32]. The properties of individual CNTs depend on their chiralities [33]. It is possible to describe the conductivity of the CNT thin films using the percolation theory that takes the geometrical properties of the CNTs into account [34]. The crucial geometrical properties are the length and diameter of the CNTs. Furthermore, the chirality of the CNT determines the type of the CNT and is another important property of CNT thin films. Based on experimental investigations of CNT networks [35], the dc electrical conductivity (σ_{dc}) of the CNT network varies as $\sigma_{dc} \sim L_{av}^{1.46}$, where L_{av} is the average bundle length.

The power law dependence found in the work by Hecht *et al.* [35] indicates that the total conductivity of the CNT network is determined by the resistances of the CNT junctions. This finding is also in accordance with the studies of conductance measurements of CNT networks probed by atomic force microscopy (AFM) [36, 37]. We also consider the CNT junctions and their conductances although some study has shown that the individual CNT also might affect the total conductivity significantly [38]. A benefit of the AFM method is the possibility to image the topography and the conductance of the CNT network simultaneously. These studies indicate that the conductance of the system does not decrease linearly with the distance from the electrode to the point where the measurement is performed. The number of interconnects in the CNT network has a great influence on the local electrical properties of the whole system. For instance, when the network comprises a small number of interconnects, the conductance stays at the same order of magnitude throughout the system but decreases abruptly at some points. The positions where the decreases in the conductance are observed correspond to the places of the CNT junctions [36]. For example, measuring the resistance of the system gives a value $0.2 \times 10^8 \Omega$ before a junction and the value of the resistance after the same junction is $2 \times 10^8 \Omega$. This means that the increase in the resistance of the network is large, of the order of $10^8 \Omega$.

In Ref. [36], the conductance drops are attributed to the crossed junctions between semiconducting and metallic CNTs. The junction consisting of a semiconducting and a metallic CNT has a significantly higher resistance than that of another junction between two metallic CNTs or two semiconducting ones. It turns out that in the CNT thin films with a large number of interconnects the behaviour of the conductance is not monotonic with the distance from the electrode. Instead, the conductance can be locally higher if the place measured contains a cluster of CNTs having several routes to the electrodes. Then finding a path with only metallic CNTs is also more probable, which improves the local conductivity. A special remark about the AFM measurements is that they enable the distinction between metallic and semiconducting CNTs. Finding completely

metallic paths and imaging them can also be carried out with the method shown in the work by Stadermann *et al.* [36]. A newer study regarding the local electrical properties of CNT networks also implies that their total conductivity is dictated by the resistances of the CNT junctions [39]. Further, the junction resistances can be reduced efficiently using acid treatment.

The effect of the length and diameter of the CNTs on the macroscale conductivity of densely packed single-walled CNTs has been examined in Ref. [40]. This work includes both experimental results and computer simulations of CNT networks. The length of the CNTs in the systems investigated computationally varies between 0.3 and 5.6 μm and the diameter of the CNT is set to a fixed value 10 nm. The CNTs form a three-dimensional spatially homogeneous network, where the orientation of each CNT is sampled from a two-dimensional planar isotropic distribution. The CNT probability distribution function is uniform in this case. The volume fraction of single-walled CNTs in the network is 60%. The simulations show that the conductivity of the CNT network can be described with a power law. It can be written as $\sigma(L) = 7.13L^{2.32} \text{ S cm}^{-1}$, where the length L is expressed in units of micrometers. The exponent 2.32 is a little larger than the previous exponent 1.46 obtained in Ref. [35]. A limitation of the model is that it cannot be applied to long CNTs ($L > 10 \mu\text{m}$) because of the intrinsic resistance of the CNTs. Moreover, the dependence of the conductivity on the diameter of the CNT is explored in Ref. [40]. Constructing CNT bundles with diameters between 3 and 30 nm and with a length of 2 μm and computing the conductivity of the entire network as a function of the diameter d results in a power law expression that can be written as $\sigma(d) = 5.23 \times 10^7 d^{-3.15} \text{ S cm}^{-1}$, where the unit of d is a nanometer. The volume fraction of CNTs in this case is assumed to be 60% so the volume fraction is the same as that of the systems used to model the influence of the length of the CNT on the conductivity. The results from the simulations related to the length dependence show that the conductivity of the CNT network decreases with increasing the diameter d of the CNTs.

The orientation of the CNTs in the CNT network is often random after the manufacturing process. Aligning the CNTs is one way of enhancing the electrical conductivity of the network. Besides investigating the influence of the length and the diameter of the CNT on the sheet conductivity, the work by Jack *et al.* [40] considers CNT networks with aligned CNTs. The conductivity parallel to the orientation of the aligned CNTs is higher than the corresponding value measured perpendicular to the CNTs.

Random networks of CNTs have been considered using a percolation model that enables the investigation of the conductivity of the system [34]. The essential parameters in this model are the lengths L_S of the individual CNTs and the channel lengths L_C . It is also important to study percolation in the network in the ballistic and diffusive regimes. The assumption of ballistic transport is valid if L_C is much shorter than the mean free path of the electron and the CNT density is below the percolation limit. If L_C is significantly larger than the mean

free path, scattering of electrons with, e.g., phonons or surface roughness can take place and the transport can be described using a diffusive model. Below the percolation threshold, both ballistic and diffusive currents approach zero when the ratio L_C/L_S is increased. Thus, the result given by both models also agrees with other studies of the length dependence.

The density of CNTs in the network is important in the case of diffusive transport [34]. The conductivity of the network is proportional to L_C^n , where n is called a conductance exponent. For high CNT densities and strong coupling between the CNTs, the conductance exponent n is close to -1.0 , which corresponds to ohmic conduction. The exponent n decreases with lowering the CNT density so the relation becomes non-linear. This occurs when the CNT density is near the percolation threshold. The findings of Ref. [34] give insight into the physical properties of the CNT network. The results are particularly useful in analysing, for instance, the conductivity of new electronic devices utilising the CNT networks.

Investigating the influence of the statistical distributions of the alignment of CNTs on the CNT network reveals that the type of the distribution and its broadening affect the total conductivity of the network remarkably. Three different statistical distributions for CNTs (rectangular, Gaussian, and Lorentzian) have been considered in a computational study by Simoneau *et al.* [41]. The main outcome of the work is that the conductivity of the network can be greatly improved by controlling the alignment of the CNTs. The highest conductivity is obtained when CNTs are positioned parallel to the conduction channel. The broadening of the distribution also influences the sheet conductivity so that there is usually a maximum when the deviation is between 10° and 30° . However, the Lorentzian distribution does not possess a similar maximum as seen in the rectangular and Gaussian distributions. Finally, it should be noticed that achieving high conductivity of the CNT thin film requires aligning the CNTs parallel to the electrode system and having an appropriate angle distribution of CNTs.

4.2 Acid doping

The influence of acids on CNTs has been considered in several previous experimental studies due to the ease and simplicity of chemical processing. Thin films or bucky papers consisting of single-walled CNTs doped with either hydrochloric, nitric, or sulphuric acid show a shift of the Fermi level [42]. Investigating the properties of CNT bucky papers treated with these Brønsted acids can be performed with X-ray induced photoelectron spectroscopy (XPS). This method enables finding the shift of the Fermi level by studying the changes in the electron core level binding energies of the elements in the system. In this case, all three acids (HCl, HNO₃, and H₂SO₄) result in a p-type doping effect, which is also called hole-doping. This means that the Fermi level shifts downwards

into the valence band. The idea of the doping process is depicted schematically in Figs. 4.2(a)–(c) for a pristine, p-doped, and n-doped semiconducting CNT system. The Fermi level is thought to lie in the middle between the valence and conduction bands in the case of a pristine semiconducting CNT.

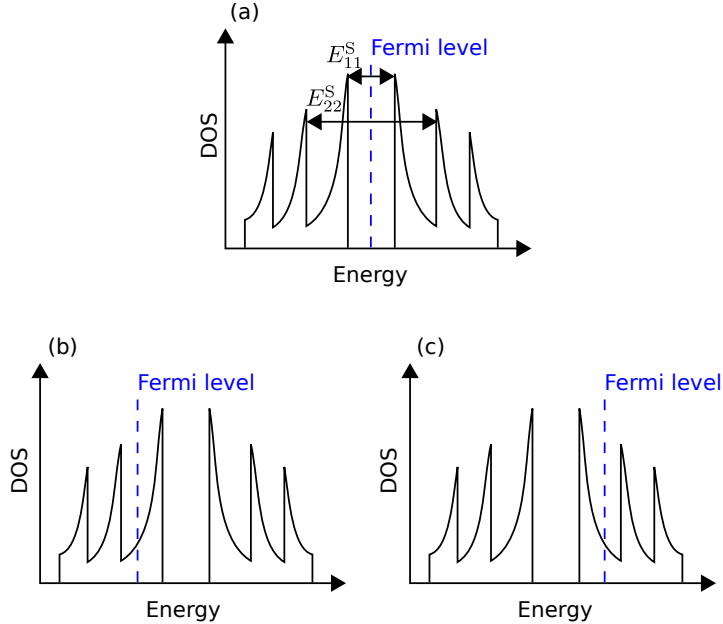


Figure 4.2. Schematic figure of the Fermi level in the DOS of (a) a pristine semiconducting CNT, (b) a p-doped semiconducting CNT, and (c) an n-doped semiconducting CNT. The transitions between the first and second van Hove singularities are shown in the DOS plot in (a).

The shifts of the Fermi level determined in Ref. [42] are 0.1, 0.2, and 0.5 eV for HCl, HNO₃, and H₂SO₄, respectively. The values of the shifts have been measured using the binding energy shifts of the C 1s core level. Besides the energy shifts, broadening of the spectral lines is observed. The authors of Ref. [42] propose that the broadening can originate from the simultaneous presence of semiconducting and metallic CNTs, defects, or from an increase of the DOS at the Fermi level. Additional studies of the S, N, and Cl core level spectra indicate that intercalation by the HNO₃ or NO₃⁻ molecules occurs between the CNTs in the bundles, which is in agreement with previous experimental work [43]. A downshift of the Fermi level due to the doping of single-walled CNTs with HNO₃ and H₂SO₄ has also been found in a study by Zhou *et al.* [44]. Consistent results are obtained with thermopower, optical reflectivity, and Raman spectroscopy measurements. No dependence of the doping on the CNT diameter is observed. Estimated values for the Fermi level downshifts are 0.35 and 0.50 eV for NO₃⁻- and H₂SO₄-doped CNT networks, respectively. These values are in good agreement with Ref. [42]. The shifts of the Fermi level of the CNT networks after the acid doping correspond to a case presented in Fig. 4.2(b), where the Fermi level

shifts downward in energy past the van Hove singularities.

An important finding of the experimental study in Ref. [44] is that the acid doping reduces the sheet resistance considerably. In addition, the resistivity of the thin film behaves differently as a function of temperature after the nitric-acid doping. The decrease in the resistivity is larger in the case of H_2SO_4 doping and the resistivity even increases at high temperatures indicating metallic behaviour.

It is also essential to investigate the impact of nitric-acid doping on the individual CNTs and CNT junctions in the thin film in order to understand the transport properties of the whole CNT network. AFM measurements of isolated CNT junctions before and after the nitric-acid doping make it possible to determine the resistance per unit length for individual CNTs and also the contact resistance of the CNT junctions [37]. Doping the CNTs with HNO_3 reduces the resistances of the junctions between the CNTs by a factor of around three. In addition, the sheet resistance of the entire thin film decreases by a factor of four after the nitric-acid doping. An important conclusion of the work by Znidarsic *et al.* is that the improvement of the conductivity of the whole structure can be attributed to hole-doping of CNTs, which decreases the tunnelling barrier heights between the contacts of CNTs. The reduction of the resistances of the CNT junctions due to the nitric-acid doping has also been confirmed by investigating the local electrical properties of the CNT networks using electrostatic force and scanning gate microscopy [45]. This work also shows that doping the CNT network with HNO_3 results in a remarkable enhancement of the conductivity of individual CNTs, which is in clear contrast to the finding of Ref. [37], where only a small reduction in the resistivity of the single CNTs after the nitric-acid doping is observed.

4.3 Other common dopants and methods to modify the properties of carbon nanotube thin films

The properties of CNT thin films can be enhanced by acid doping but a marked challenge related to the acid treatment is stability. For instance, doping the CNT thin films with HNO_3 leads to a significant increase in the conductivity immediately after the doping but thereafter the conductivity decreases rapidly due to the evaporation of the acid [46]. The degradation of the doping effect can be confirmed using UV-vis-NIR absorption spectroscopy, Raman spectroscopy, or XPS.

Besides the acids, the CNT networks can be doped with various compounds such as AuCl_3 [47], MoO_x [48], and $\text{CuCl}_2/\text{Cu}(\text{OH})_2$ redox [49]. The use of AuCl_3 as a p-type dopant for CNT thin films has been reported [47]. In this case, the van Hove transitions E_{11}^S , E_{22}^S , and E_{11}^M disappear in the UV-vis-NIR absorption spectroscopy indicating p-type doping. The E_{11}^S and E_{22}^S transitions are depicted in Fig. 4.2(a). Additional studies employing Raman and ultraviolet

photoelectron spectroscopy also reveal that the system becomes p-doped due to the AuCl_3 doping. A downshift of the Fermi level up to 0.42 eV is measured and the resistivity of the CNT thin film decreases by approximately 90% if the doping concentration is high [47]. Thus, the conductivity of the CNT thin film improves by a factor of around ten in this case.

There is a significant number of methods that are suitable for doping CNTs nowadays. The doping atoms or molecules do not always bind to the outer surface of the CNT. Instead, they can also locate inside the CNTs. For example, iodine can be used to improve the conductivity properties of CNT thin films such that the sheet resistance decreases by an order of magnitude after the iodine doping [50]. In an experimental and computational study by Fan *et al.* [51], the iodine atoms have been found to form helical chains inside single-walled CNTs. These structures have been investigated using atomic resolution Z-contrast scanning transmission electron microscopy. The microscopy images show helices the structure of which is in accordance with DFT calculations employing LDA and norm-conserving pseudopotential plane waves. To keep the number of atoms in the system small enough, investigating iodine chains on flat graphene sheets or on curved graphene sheets gives enough information on the optimal atomic structure of the real CNT system. Three different configurations where the lattice of the CNT and the iodine spacing are almost commensurate are considered. The longest two periods of the computationally studied iodine chains correspond to experimentally observed structures examined with microscopy.

Iodine chains inside CNTs have been explored in Ref. [52] both experimentally and computationally. In that study, one-dimensional iodine chains are found to form different kinds of phases inside the CNTs. Besides equidistant chains, chains consisting of iodine dimers and trimers can also be observed inside the CNTs as investigated using high-resolution scanning transmission electron microscopy. Transitions between the dimer and trimer phases can take place. The trimerised phase turns out to be interesting because the calculations show that the band gap opens in this case, which indicates the formation of a charge density wave in the system.

The filling of CNTs with one-dimensional copper halide crystals has been investigated with several experimental methods and the copper halides have been shown to work as acceptors [53]. In this case, single-walled CNTs are filled with CuCl , CuBr , or CuI by a capillary technique. Then the work functions of the nanostructures are determined and a downshift of the Fermi level because of the doping is observed. This downshift indicates charge transfer from the CNTs to the 1D crystals. According to the experiments in Ref. [53], the nanocrystals bind to the CNT walls due to hybridisation between C $2p_z$ π and Cu $3d$ orbitals. This hybridisation results in new localised states. The DOS of these new localised states, charge transfer in the system, and the downshift of the Fermi level rise when the electron affinity of the halogen atom increases. Therefore, the highest value is obtained for a CuCl crystal inside the CNT.

Doping of CNT thin films with CuCl and iodine has also been considered

in an experimental study by Tsebro *et al.* [54]. The work shows the temperature behaviour of the electrical resistance of the CNT thin films for pristine and doped samples. The sheet resistance as a function of temperature has a minimum that shifts towards lower temperatures because of the doping. In addition to the experiments, Tsebro *et al.* [54] also analyse the data by using a heterogeneous model consisting of two contributions to the resistance. The first part of the model describes the conductances of the junctions and is related to fluctuation-assisted tunnelling. The second contribution is needed to explain the conductivity of individual CNTs or bundles of the network and describes backscattering of charge carriers by low-energy phonons. This term, however, is important only at low temperatures.

An essential result of Ref. [54] is that the sheet resistance of the CNT network is mainly determined by the first part of the model accounting for the junction resistances, in agreement with previous experimental investigations [39]. Furthermore, the sheet resistance decreases by one order of magnitude and the doping effect also remains stable in air a long time. According to the measurements, the sheet resistance¹ is approximately $100 \Omega/\square$ after the doping and is close to that of a commercial indium tin oxide thin film. It turns out that the doping of CNT thin films causes a downshift of the Fermi level into the valence band. The value of the downshift is 0.6 and 0.9 eV for iodine- and CuCl-doped CNT thin films, respectively.

A remarkable increase in the conductivity of CNT thin films doped with MoO_x has been observed [48]. The resistivity of the CNT network decreases approximately by a factor of two when MoO_x is deposited by thermal evaporation. After annealing the MoO_x-doped CNT thin film for a few hours in argon, the resistivity of the network reduces by a factor of 5–7 with respect to the undoped and unannealed network. The doping effect can be seen as a suppression of the van Hove transitions. Further, performing XPS measurements of the MoO_x-doped CNT thin films shows that the Mo⁶⁺ oxidation state dominates the Mo 3d spectrum and the Mo⁴⁺ state cannot be seen before annealing. When the sample has undergone an annealing process, Mo⁶⁺ remains the dominant oxidation state but the Mo⁴⁺ and intermediate ones become visible. This indicates chemical reduction of MoO_x meaning that it receives electrons from the CNT. Additionally, the MoO_x doping is stable thermally and also shows a very good chemical stability. According to Ref. [48], this method can be used to fabricate MoO_x-CNT composites with sheet resistances of $100 \Omega/\square$ at 85% transmittance.

Doping CNT thin films with CuCl₂/Cu(OH)₂ redox has been shown to improve the conductivity of the network markedly [49]. A reduction of the resistance by a

¹The unit of the sheet resistance is commonly Ω/\square and this unit is useful in the measurements of thin films having a uniform thickness. If the shape of the thin film is a square, the resistance of the system is always the same regardless of the area of the square. Thus, the unit is defined as ohm per square. In the case of a system that is, e.g., four units long and one unit wide, the resistance of the system is four times the resistance of a square where the side length is one unit. This example shows the relation between the resistances of square and non-square systems.

factor of 4.4 has been found. Thus, the resistance of the CNT thin film decreases from over 300 to 69.4 Ω/\square at 90% transmittance after treating the CNT thin film with the redox dopant. A great advantage of this redox doping, for instance, over the acid one is the stability. Keeping the thin film in ambient condition for one year only results in a slight increase in the sheet resistance. The measured value of the sheet resistance is 73.5 Ω/\square after one year.

The characteristics of the $\text{CuCl}_2/\text{Cu}(\text{OH})_2$ doping can be investigated by using the Raman or UV-vis-NIR spectroscopies. After doping the CNT thin film with the $\text{CuCl}_2/\text{Cu}(\text{OH})_2$ redox, a remarkable decrease in the Raman intensity and blue shifts in the G and G' bands of the Raman spectra are observed indicating p-type doping. This redox functionalisation can also be used to fabricate solar cells as presented in Ref. [49]. In this case, the redox-functionalised CNT thin film could work as an efficient hole-transporting layer in a CNT/Si solar cell. The power conversion efficiency (PCE) of a pristine CNT/Si solar cell is rather low, 6.6%. The $\text{CuCl}_2/\text{Cu}(\text{OH})_2$ functionalisation increases the PCE of the CNT/Si solar cell by 115% and the measured value after the doping process is 13.77%. Moreover, the open-circuit voltage, short-circuit current density, and fill factor enhance significantly because of the redox functionalisation. They do not change so much in the ambient conditions after one year and the PCE of the doped CNT/Si solar cell even improves a little during that time. Therefore, the stability of the redox-functionalised CNT thin film is also good for device applications including new types of solar cells.

Besides the doping methods discussed in this section, a few n-type dopants for the CNT have also been developed [55]. However, the stability and longevity of the n-type doping has been a significant problem. Early studies of CNT systems indicate that single-walled CNT bundles can be made n-doped with potassium that works as a donor in the system [56]. An interesting finding is also a possibility to obtain n-type doping in CNTs by using ordinary salts with crown ethers. In addition, this type of doping shows remarkable stability in air longer than one month [57]. Another study [58] shows that n-type doping of CNTs can also be carried out by encapsulating cobaltocene inside the CNTs. Doping of CNTs with 1,2,4,5-tetrakis(tetramethylguanidino)benzene has also turned out to be a promising method to make n-doped CNTs [59]. In particular, these systems could be used in transistor applications.

Another method to modify the properties of CNT networks is to use molecular linkers between the CNTs as shown in Ref. [60]. The molecular linkers can be either electron donors or acceptors. The CNT thin film with molecular linkers has diode-like behaviour. The mechanical and electronic properties of CNT networks improve as a result of the linking process [61]. The use of molecularly linked CNTs as an oil filter has been demonstrated [62]. Moreover, joining of two parallel multi-walled CNTs has been carried out with electron irradiation [63]. These welded systems may turn out to be useful in applications where CNTs are utilised.

5. Carbon nanotube junctions with linker atoms

A new approach for enhancing the electrical properties of CNT thin films is modifying them chemically with group 6 TM atoms [64, 65]. Previous experimental investigations have shown that the electrical conductivity of both semiconducting and metallic CNT networks improves remarkably when they are treated with Cr atoms. The improvement of the conductivity, however, depends on the thickness of the CNT thin film as well as on the chiralities of CNTs. The enhancement of the conductivity is larger if the CNT network is very thin. Furthermore, the effect of Cr atoms on the network of semiconducting CNTs is more significant than on one consisting of metallic CNTs.

The enhancement of the conductivity of CNT thin films due to the group 6 TM atom deposition can be attributed to covalent, organometallic hexahapto (η^6) bonds between the CNTs and the TM atoms [64]. The group 6 TM and carbon atoms have six valence electrons. By forming covalent bonds with the carbon rings on the sidewalls of the CNTs, the group 6 TM atoms obtain the favourable 18-electron configuration, which means that they have a closed shell. A particular objective of the work performed in Publication I is to model the systems that form when, for instance, Cr atoms bind to the sidewalls of the CNTs. Our model is a continuation of the previous computational study by Li *et al.* [66]. The authors of Ref. [66] have considered a junction of two semi-infinite CNTs linked by various metal atoms. Furthermore, an increase in the conductance of a similar junction of two parallel CNTs with a gold nanoparticle between them has also been found in another study [67]. In our work, we study a four-terminal system that consists of two infinite CNTs connected by a TM linker atom. Therefore, our system has the advantage that the ends of the CNTs do not cause unnecessary scattering and the system also makes it possible to examine electron transport through individual CNTs in the junction while only transport through the junction can be studied in the case of a two-terminal system with semi-infinite CNTs. The CNT junctions investigated in Publication I and their electronic transmission functions are presented in this chapter. Furthermore, the charge densities of some eigenstates of the system are depicted.

5.1 Structure of the CNT junction

The CNT junctions investigated in Publication I consist of two infinite single-walled armchair CNTs. The CNTs are placed perpendicular to each other and connected by either one Cr, Mo, or W atom. We mainly study a junction of two (8,8) CNTs but consider also junctions of two (5,5) or (11,11) CNTs. The CNTs are rotated so that the linker atom lies just above the centres of the carbon rings on the outer surfaces of the CNTs. Then the formation of the hexahapto system can occur as described at the beginning of the chapter. The structure of the junction of two (8,8) CNTs with a Cr linker atom is shown in Fig. 5.1. This system works as a computational model of the CNT junctions, where the lengths of the CNTs are infinite.

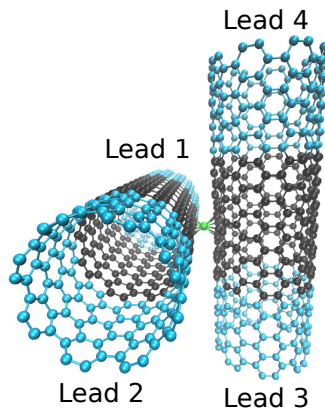


Figure 5.1. A junction between two metallic (8,8) CNTs linked with a Cr atom. The atoms with light blue colour belong to the lead regions. The lead numbering is also shown in the figure.

Optimisation of the atomic structures of the CNT junctions needs to be carried out before computing electronic transmission functions for them. All computational models of the CNT junctions examined in the present work are similar to the system depicted in Fig. 5.1 and the ends of the CNTs form the lead regions indicated by a different colour in the same figure. The actual optimisation of the structure is performed so that the distance between the CNTs in the junction is varied and the system is relaxed using different distances until the configuration with the lowest energy has been found. The positions of the lead atoms are fixed during the relaxation calculations since the leads should represent pristine CNTs without deformations. The optimal distance is obtained by fitting a second-degree polynomial to the total energy values of the relaxed systems. This way of optimising the CNT-CNT distance in the junction is also used in other CNT junctions investigated in this work. However, the displacements of the atoms in the junction region turn out to be relatively small. Therefore, part of the

CNT junction systems are not relaxed fully but only the CNT-CNT distance is optimised by varying the positions of the CNTs and finding the energy minimum. The distance $d_{\text{CNT-CNT}}$ between the CNTs in the junction is defined as

$$d_{\text{CNT-CNT}} = d_{\text{axes}} - r_1 - r_2, \quad (5.1)$$

where d_{axes} denotes the distance between the axes of the CNTs, r_1 is the radius of the first pristine CNT, and r_2 is the radius of the second pristine CNT.

The optimal distance between two pristine (8,8) CNTs is 2.46 Å. With a Cr linker atom, the CNT-CNT distance increases to 2.56 Å. When the CNTs are connected by a Mo or a W atom, the corresponding distance is larger than in a CNT junction with a Cr linker atom and is nearly 3 Å. The difference comes from the larger size of the linking atom. The diameter of the CNT also affects the optimal CNT-CNT distance that decreases with increasing the diameter of the CNT. The CNTs are closer to each other when their diameters are larger because the curvature of the CNTs is then lower.

Stability of the CNT junction with a TM linker atom is also relevant and can be considered by computing the binding energy for the TM atom between two CNTs. However, a calculation of the binding energy for a single TM atom is first required. The binding energy $E_{b,1}$ for an atom adsorbed on a CNT can be expressed as

$$E_{b,1} = E_{\text{T}}[\text{CNT-X}] - E_{\text{T}}[\text{CNT}] - E_{\text{T}}[\text{X}]. \quad (5.2)$$

The energy $E_{\text{T}}[\text{CNT-X}]$ in Eq. (5.2) denotes the total energy of the CNT with an X atom. Correspondingly, $E_{\text{T}}[\text{CNT}]$ and $E_{\text{T}}[\text{X}]$ are the total energies of the pristine CNT and the single X atom, respectively. The X atom in Eq. (5.2) can also be an X molecule. The binding energy for an X linker atom between two CNTs is defined as

$$E_{b,2} = E_{\text{T}}[\text{CNT-X-CNT}] - E_{\text{T}}[\text{CNT}] - E_{\text{T}}[\text{CNT-X}], \quad (5.3)$$

where $E_{\text{T}}[\text{CNT-X-CNT}]$ is the total energy of the CNT junction with an X linker atom and the meaning of the two other terms is the same as in Eq. (5.2). In Publication I, the binding energy $E_{b,2}$ for the Cr linker atom is determined and its value is -4.2 eV. Thus, the CNT-Cr-CNT system is stable.

5.2 Electronic transmission functions and charge densities

Junctions of two metallic armchair (8,8) CNTs with group 6 TM linker atoms are first relaxed and electronic transmission functions are computed for the optimised structures. Because of the closed-shell structure, spin can be neglected in the transport calculations. Intra- and intertube electronic transmission functions for CNT junctions with and without TM linker atoms are presented in Figs. 5.2(a) and 5.2(b).

The transport calculations for a junction of pristine (8,8) CNTs give an intratube transmission function (see Fig. 5.2(a)) that consists of several steps

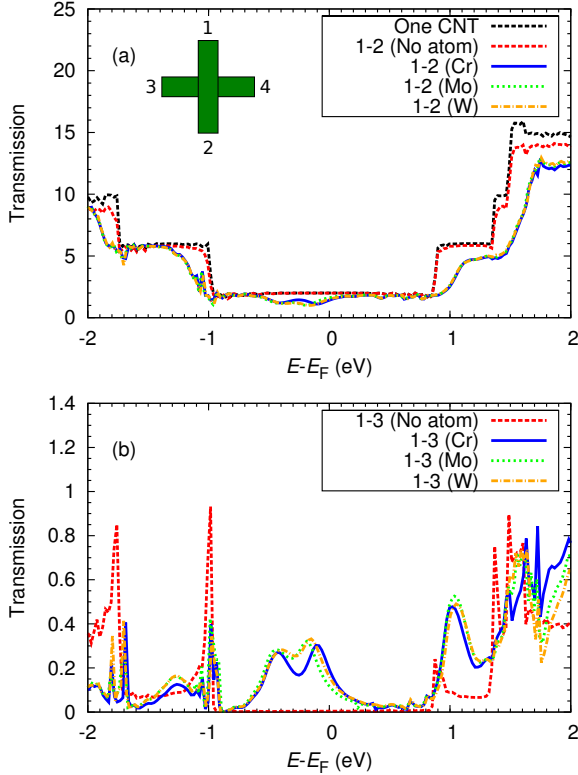


Figure 5.2. (a) Intratube and (b) intertube transmission functions for CNT junctions with different linker atoms. The transmission function for a pristine individual CNT is also shown in the upper plot. The numbers of the leads are presented in the inset.

and has a finite value close to the Fermi level. This means that the system is conductive and metallic. Without the linker atom, the values of the intertube transmission function in Fig. 5.2(b) are close to zero in a broad energy region in the vicinity of the Fermi level and also remain low outside this region except for a few high peaks that originate from the high density of states of individual pristine CNTs. The intra- and intertube transmission functions for the junction of two pristine (8,8) CNTs resemble the previous computational results [68].

A significant enhancement of the intertube transport is observed when the (8,8) CNTs are linked with a TM atom as shown in the intertube transmission functions in Fig. 5.2(b). There are two rather broad peaks below the Fermi level and the tail of the first peak just below the Fermi level extends above it. All three TM atoms (Cr, Mo, and W) result in similar double peak structures in the Fermi energy regime. The TM linker atoms do not lower the intratube transport significantly, which can be seen in Fig. 5.2(a). Only a small number of dips appears in the intratube transmission functions and their values remain close to those of the intratube transmission function for the pristine (8,8) CNT. This is also a great advantage of linking the CNTs with TM linker atoms.

There are differences between the transmission functions of Publication I and those obtained in a study by Li *et al.* [66]. In Ref. [66], the linking atoms lead to remarkably broader peaks in the neighbourhood of the Fermi level. We can attribute the differences to a few reasons. The chiralities of the CNTs in Ref. [66] are (5,5) instead of (8,8) that is chosen for our systems. Moreover, Li *et al.* have considered a junction of semi-infinite and parallel CNTs. Because the CNTs are semi-infinite, quasilocalsed end states can form in the junction. We have also considered the effect of the diameter of the CNT on the transport and found that the size influences, e.g., the distance between the peaks in the intertube transmission functions. However, the results from Publication I are in qualitative agreement with the previous reports [66].

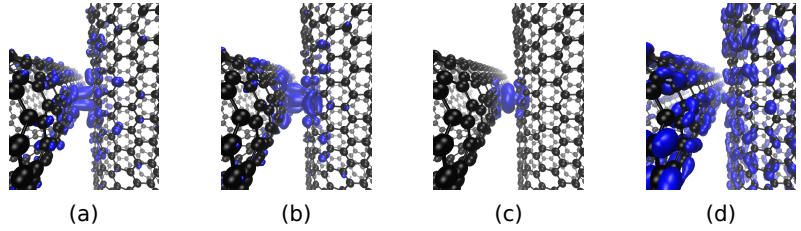


Figure 5.3. Charge densities of (a) the OHEE₃, (b) the OHEE₂, (c) the OHEE₁, and (d) the ULEE₁ eigenstates for the junction of two (8,8) CNTs linked with a Cr atom. The blue isosurface represents the charge density and the value of the isosurface is the same for all eigenstates.

Valuable information about the origin of the peaks in the intertube transmission curves in Fig. 5.2(b) can be obtained by examining the charge densities of the eigenstates in the vicinity of the Fermi level. The peaks in the intertube transmission functions between $E - E_F \approx -0.8$ eV and $E - E_F \approx 0.2$ eV are associated with an unoccupied low-energy eigenstate (ULEE₁) and three occupied high-energy eigenstates (OHEE₁, OHEE₂, and OHEE₃). The electron densities of these states of a CNT junction with a Cr linker atom are represented by blue isosurfaces in Figs. 5.3(a)–(d).

The ULEE₁ lying approximately 0.1 eV above the Fermi level does not show remarkable hybridisation between the Cr and CNT orbitals as presented in Fig. 5.3(d). In contrast, a large amount of charge lies on the CNTs. In the case of the OHEE₁ (see Fig. 5.3(c)), the state is located at the Fermi level and toroidal regions of electron density appear around the linker atom. There is only minimal hybridisation between the Cr and CNT orbitals in the junction region. The shape of the isosurface of the OHEE₁ resembles the $3d_{z^2}$ orbital. Interestingly, the orbitals of the OHEE₂ and OHEE₃ have four longitudinal regions that fill the whole junction area, which is a clear sign of hybridisation. It resembles that observed in a system of two polyacene molecules connected by a Cr atom and indicates coupling of the carbon π orbitals to the d orbitals of the Cr atom [66].

By studying the shapes of the orbitals, we can identify their types. A study by Rayon *et al.* shows the orbital structure of a bis(benzene)chromium (CrBz₂) molecule that acts as a model system for CNT junctions with Cr linker atoms [69].

The highest occupied molecular orbital (HOMO $a_{1g}(\sigma)$) of the CrBz_2 molecule corresponds to the OHEE_1 in Fig. 5.3(c). Similarly, we can link the OHEE_2 and OHEE_3 with the HOMO-1 $e_{2g}(\delta)$ states of the same molecule. Finally, the lowest unoccupied molecular orbital LUMO e_{2u} of the CrBz_2 system can be attributed to the ULEE_1 . In Ref. [69], an energy partition scheme has been employed to analyse the type and structure of the metal-ligand bonding in the CrBz_2 molecule. According to the bonding analysis, the Cr-C bond in CrBz_2 is 37.9% electrostatic and 62.1% covalent, which is also in agreement with small charge transfer found in the junctions of CNTs with TM linker atoms as shown in Publication I. Another essential finding of Ref. [69] is that the largest contributions to the orbital interactions in the CrBz_2 molecule originate from the $\text{Cr} \rightarrow \text{Bz}_2$ δ -backdonation. Therefore, this molecule can be regarded as a δ -bonded molecule.

6. Molecular doping of carbon nanotubes and carbon nanotube junctions

An alternative and promising way of tuning the properties of CNTs is doping them chemically, e.g., with atoms or molecules. In the present work, we consider charge transfer doping of single-walled CNTs with gold chloride and nitric acid molecules. In particular, the doping efficiencies of these molecules are determined by computing band structures for the doped CNT systems. Besides the band structures, electronic transmission functions for single doped CNTs and junctions consisting of two CNTs doped with molecules are investigated.

The topic of the first part of this chapter is the doping of semiconducting (10,0) CNTs with AuCl_4 anions. The AuCl_4 molecule is called an anion in this work. We compute the band structures both with the usual PBE and the HSE06 hybrid exchange-correlation functionals. Further, the first part deals with junctions of two semiconducting CNTs with AuCl_4 anions. These systems resemble a little those examined in Publication I but the CNTs in the junctions are covered with molecules and there is not always a linking molecule between the CNTs. After presenting the most important results from Publication II, we consider CNTs doped with NO_3 molecules, which is the topic of Publication III. The last part of this chapter presents a concise summary of the most relevant results of Publication III. In this case, both semiconducting and metallic CNTs with NO_3 molecules are examined. In addition to individual CNTs, junctions of two metallic or two semiconducting CNTs with doping are studied in this work. Finally, we consider a junction of a NO_3 -doped semiconducting and a NO_3 -doped metallic CNT.

6.1 Semiconducting carbon nanotubes with AuCl_4 molecules

Experimental investigations of the interaction of the HAuCl_4 solution with CNTs have indicated spontaneous formation of Au nanoparticles on the sidewalls of the CNTs [70]. These nanoparticles are related to a direct redox reaction between the CNTs and the metal ions. The difference between the relative potential levels of the CNT and the AuCl_4 anion explains why electron transfer from the CNT to the gold ions takes place, which causes reduction of the metal

ions to atoms that form Au nanoparticles. In this reaction, the CNTs donate electrons and become p-doped. As a result, the conductivity of the CNT network increases simultaneously. This improvement of the conductivity of the CNT thin film has also been confirmed in another experimental study by Kim *et al.* [47] as presented in another section dealing with the CNT doping. The doping compound in that study was AuCl_3 that corresponds to HAuCl_4 used in Ref. [70]. The benefit of AuCl_3 compared with other dopants is the high doping efficiency [71]. The doping efficiency in this thesis is defined as the charge transferred from the anion to the CNT. Hence, this compound has been investigated in more detail.

A particular objective of this work is describing the mechanism of AuCl_3 doping using computational models. The study of Ref. [47] indicates that chloride anions play an important role in the AuCl_3 doping. In a newer study [72], the results given by DFT calculations showed that the Cl^- anions do not result in a stable doping effect since it depends on the relative positions of the anions on the CNT remarkably. In this case, the instability is related to the Peierls effect. Instead, AuCl_4^- anions adsorbed on the semiconducting (10,0) CNTs have been shown to cause charge transfer from the CNTs to the anions. Then the CNTs become p-doped. The study by Murat *et al.* [72] works as a starting point for our computational studies.

Computing the band structures for AuCl_4^- -doped CNTs is performed as a function of the concentration of the AuCl_4^- anions. For these calculations and also for the transport calculations of the junctions of doped CNTs, we define a computational unit cell that consists of four primitive unit cells of a (10,0) CNT and a few AuCl_4^- anions on the outer surface of the CNT. The number of the AuCl_4^- anions is varied between zero and four. A schematic figure of the computational unit cell is shown in Fig. 1 in Publication II. Construction of the computational unit cell requires finding the adsorption geometry of the anion on the CNT. The optimal geometry is determined by relaxing the atoms of the computational unit cell with one AuCl_4^- anion that is placed on a few different highly symmetric sites where the adsorption can take place. However, the changes in the total energies of the systems are minimal when different adsorption geometries are considered. Therefore, we always place the anion on the CNT so that the Au atom lies above a C atom. This configuration is also stable as shown by computing the binding energy for a AuCl_4^- anion on a (10,0) CNT. The value of the binding energy for the AuCl_4^- anion is obtained by using Eq. (5.2) and is -1.38 eV.

The band structures for pristine (10,0) CNTs in Figs. 6.1(a) and 6.1(b) show that the system is a semiconductor with a direct band gap at the Γ point. The band gap determined with PBE is 0.77 eV and the corresponding value computed with HSE06 is 0.97 eV. When the computational unit cell includes a (10,0) CNT with one AuCl_4^- anion, a downshift of the Fermi level relative to the top of the valence band is found in the band structures computed with PBE and HSE06 in Figs. 6.1(c) and 6.1(d), respectively. The downshift of the Fermi

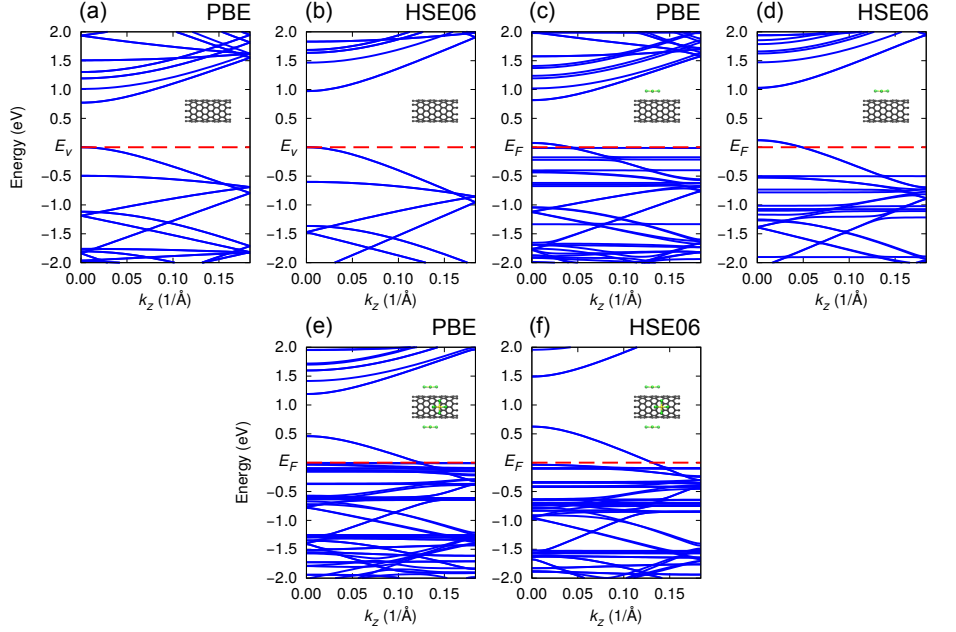


Figure 6.1. Band structures for pristine and AuCl_4 -doped (10,0) CNTs: (a)–(b) A pristine (10,0) CNT, (c)–(d) (10,0) CNT with one AuCl_4 anion in the computational unit cell, and (e)–(f) (10,0) CNT with four AuCl_4 anions in the computational unit cell. The top of the valence band and the Fermi level are denoted by a red dashed line. The insets show the structures of the computational unit cells. The functional of the calculation is also presented above each band plot.

level is larger in the case of the HSE06 functional. The band structures have several dispersionless bands coming from the localised molecular states. These dispersionless bands are located close to the Fermi level in the case of the PBE band structures. Changing the functional to HSE06 leads to a shift of the molecular bands toward lower energies, which can be seen in Figs. 6.1(d) and 6.1(f). The self-interaction error can be decreased by using the HSE06 hybrid functional, which is seen as downshifts of the energy bands in the band structures. Furthermore, the shift of the Fermi level down in energy becomes larger with increasing the concentration of the AuCl_4 anions.

The downshift of the Fermi level indicates charge transfer from the CNTs to the AuCl_4 anions meaning that the CNTs become p-doped. We can calculate the doping efficiency of the AuCl_4 anions by considering the band structures. First, we look for the crossing points of the Fermi level and the uppermost valence band. An estimate for the doping efficiency is obtained by measuring the distance from the Γ point to the intersection point, dividing this distance by the maximum k_z value, and finally multiplying the ratio by four. The multiplier four originates from the twofold spin and band degeneracies of the uppermost valence band of the semiconducting (10,0) CNT. The method introduced in Publication II for determining the doping efficiency of AuCl_4 anions can also be applied to

NO_3 molecules in Publication III. The doping efficiencies for the AuCl_4 anions on (10,0) CNTs are listed in Table 6.1.

Table 6.1. Doping efficiency in AuCl_4 -doped (10,0) CNTs as a function of the number of anions N_{AuCl_4} . The results are shown for both the PBE and HSE06 functionals.

| N_{AuCl_4} | Functional | Doping efficiency per anion (e) |
|---------------------|------------|---------------------------------|
| 1 | PBE | 0.9 |
| 1 | HSE06 | 1.1 |
| 2 | HSE06 | 1.1 |
| 4 | PBE | 0.7 |
| 4 | HSE06 | 0.7 |

The values in Table 6.1 show that the doping efficiencies for the AuCl_4 anions are larger when performing the calculations with HSE06. This can also be verified by comparing the band structures computed with PBE and HSE06. The doping efficiency for one AuCl_4 anion, determined with the method described earlier in this section, is 0.9 electrons per anion if the PBE functional is used in the calculation. The corresponding value computed with HSE06 is 1.1 electrons. Interestingly, the doping efficiency decreases significantly when the number of anions in the computational unit cell is increased. The charge transfer between the CNT and the anion is approximately 0.7 electrons in the case of four AuCl_4 anions on the CNT. The lowering of the doping efficiency can be attributed to the enhanced hybridisation between the molecular orbitals of the CNT and the AuCl_4 anions. In addition, the character of the bonds between the CNT and the anions changes from ionic to more covalent when the concentration of the doping anions is high. An essential finding of the AuCl_4 -doped systems is that the Fermi level of the highly doped systems shifts near flat CNT bands and dispersionless molecular states. As a result, the Fermi level can be pinned to the van Hove singularity. This kind of pinning suggests that the doping effect is robust so it is possible to maintain the doping effect despite small changes in the concentration of AuCl_4 anions.

In addition to the band structures, electron transport through individual semiconducting (10,0) CNTs with AuCl_4 anions is investigated. The individual (10,0) CNT with doping is constructed using the computational unit cells of the doped systems in the insets in Fig. 6.1. These unit cells are placed consecutively so that the total length of the whole transport system is three times that of the basic computational unit cell. This system represents the real one well because both the leads and the middle unit cell forming the scattering region are similarly doped. Electronic transmission functions for semiconducting (10,0) CNTs with and without AuCl_4 anions are shown in Fig. 6.2.

The transmission function for a pristine semiconducting (10,0) CNT shows a step-like structure with a gap indicating semiconducting behaviour. Computing

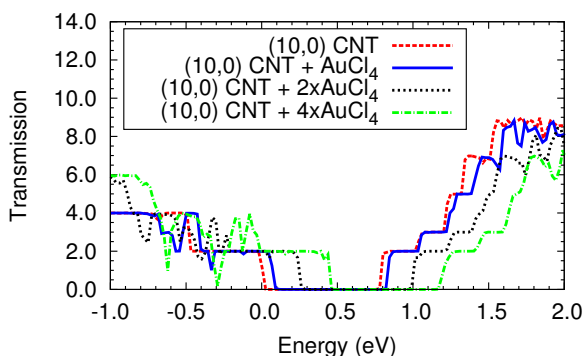


Figure 6.2. Transmission functions for a pristine (10,0) and AuCl_4 -doped (10,0) CNTs. The Fermi level is at the energy zero.

the electronic transmission function for the computational unit cell of a (10,0) CNT with one AuCl_4 anion results in a curve that is shifted toward higher energies by 0.1 eV. An increase in the dopant concentration causes even larger upshifts. These results mean that the originally semiconducting system becomes metallic. Simultaneously, several dips originating from scattering due to the anions appear in the transmission curves. In addition, the number of dips is smaller at higher energies because of the absence of molecular states.

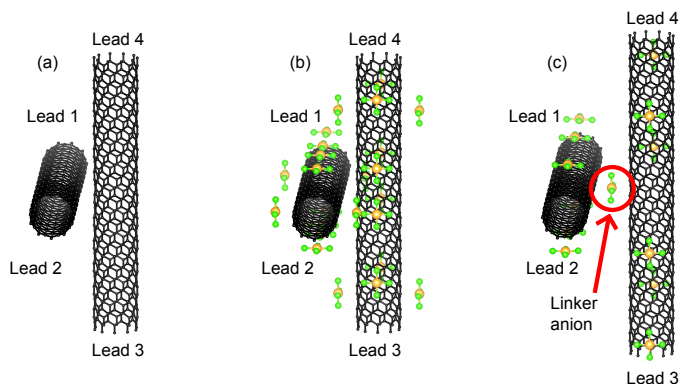


Figure 6.3. Junctions of (a) two perpendicular pristine (10,0) CNTs, (b) two perpendicular (10,0) CNTs with large concentration of AuCl_4 anions, and (c) two perpendicular AuCl_4 -doped (10,0) CNTs with a linking AuCl_4 anion.

To study the influence of AuCl_3 doping on the conductivity of CNT networks, we consider different kinds of CNT junctions without and with AuCl_4 anions. The three CNT junctions studied in Publication II are presented in Figs. 6.3(a)–(c). Before calculating the transmission functions for the CNT junctions, their atomic structures have to be optimised. A junction of two pristine (10,0) CNTs is relaxed according to the method applied for determining the optimal structures of junctions of metallic (8,8) CNTs with linker TM atoms examined in Publication

I. Hence, the positions of the lead atoms are fixed and the remaining carbon atoms in the junction region are allowed to move. The distance between the CNTs is varied and the relaxation of the systems is carried out at each distance separately. Thereafter, we can find the optimal distance by looking for the minimum of the total energies. The optimal distance $d_{\text{CNT-CNT}}$ between two pristine (10,0) CNTs is determined both with the Tkatchenko-Scheffler van der Waals correction and without it. If the van der Waals correction is employed in the relaxation calculations, the distance $d_{\text{CNT-CNT}}$ is 2.63 Å. Repeating the optimisation calculation without the correction leads to a distance of 3.68 Å. Hence, it is important to include the van der Waals correction when the CNT-CNT distance in the CNT junction is optimised.

The atomic structure of the other junctions in Figs. 6.3(b) and 6.3(c) are not relaxed fully due to high computational cost. Furthermore, the displacements of the carbon atoms in the junction of two pristine (10,0) CNTs are relatively small so the full relaxation of the other two doped systems is not needed. Contrary to the optimisation method used to find the distance $d_{\text{CNT-CNT}}$ for the junction in Fig. 6.3, we set $d_{\text{CNT-CNT}}$ in the system shown in Fig. 6.3(b) to the value 2.63 Å, the same as that obtained for a junction of pristine (10,0) CNTs. Then the AuCl_4 anions are placed on the (10,0) CNTs so that the concentration of the AuCl_4 anions corresponds to that of the computational unit cells with the largest numbers of anions in the insets in Figs. 6.1(e) and 6.1(f).

The last junction differs from the second one. In the third junction in Fig. 6.3(c), the anion concentration of the CNTs is slightly smaller and moreover the CNTs are linked with a AuCl_4 anion. The distance between the CNTs in this system is optimised so that we vary the CNT-CNT distance but do not let the atoms move relative to each other. The optimal distance $d_{\text{CNT-CNT}}$ is obtained by finding the energy minimum of the total energy values given by basic ground state calculations and is 6.69 Å. We have also investigated the displacements of the AuCl_4 anions in the junction of two AuCl_4 -doped (10,0) CNTs during the first few relaxation steps in the case of the system shown in Fig. 6.3(b). The relaxation calculations show that the anions tend to move toward the centre point of the junction region. Therefore, linking of the CNTs with AuCl_4 anions is expected to occur in the doping process and it is also essential to consider the junction in Fig. 6.3(c).

Four-terminal electron transport calculations are carried out for the three CNT junctions displayed in Figs. 6.3(a)–(c). The intra- and intertube transmission curves for a junction of two perpendicular pristine (10,0) CNTs are presented in Fig. 6.4. Correspondingly, the results of the transport calculations for a junction of two perpendicular AuCl_4 -doped (10,0) CNTs linked with a AuCl_4 anion are shown in Fig. 6.5. The transmission functions for the second junction in Fig. 6.3(b) are not shown because the results are for the valence band region qualitatively similar to those calculated for the junction of two AuCl_4 -doped (10,0) CNTs with a linker anion.

The intratube transmission function for the junction of two pristine semi-

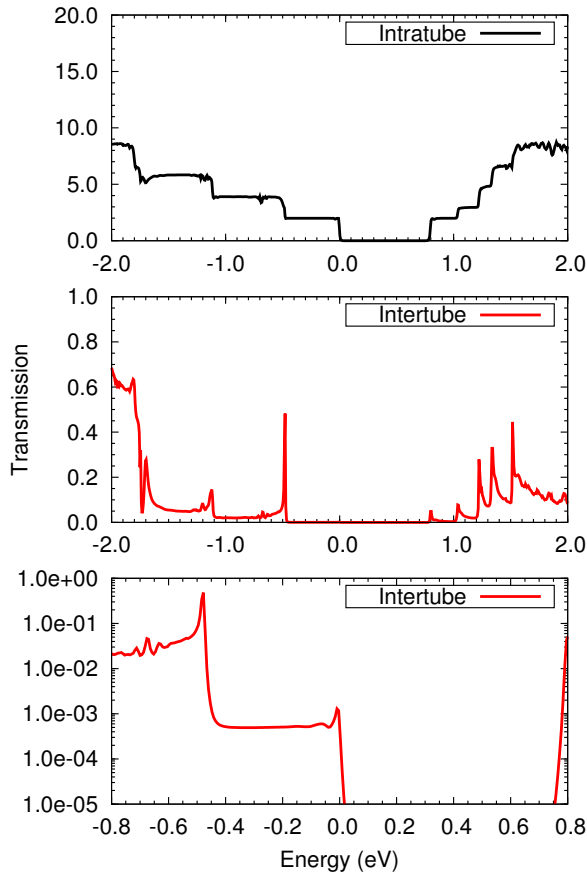


Figure 6.4. Intratube (top panel) and intertube (middle and bottom panels) electronic transmission functions for a junction of two pristine (10,0) CNTs. All curves have been shifted so that the energy zero lies at the top of the valence band of a pristine (10,0) CNT. The bottom panel shows the intertube transmission function on the logarithmic scale.

conducting (10,0) CNTs in the topmost panel of Fig. 6.4 resembles that for an individual pristine (10,0) CNT in Fig. 6.2. There are multiple steps representing discrete energy levels in the curve and it does not have any significant disturbances coming from the other CNT in the junction. The conductance of the junction of two pristine (10,0) CNTs is low as can be seen in the intertube transmission curves in Fig. 6.4 and the values of the intertube transmission functions are small in a wide energy region. The curve, however, has numerous peaks and they are located at the same energies as those of the steps in the intratube curve. Interestingly, the shape of the intertube electronic transmission function looks like the DOS for a one-dimensional electron gas. In other words, the system comprising pristine (10,0) CNTs does not conduct electricity well without any chemical treatment or an applied bias voltage, for example.

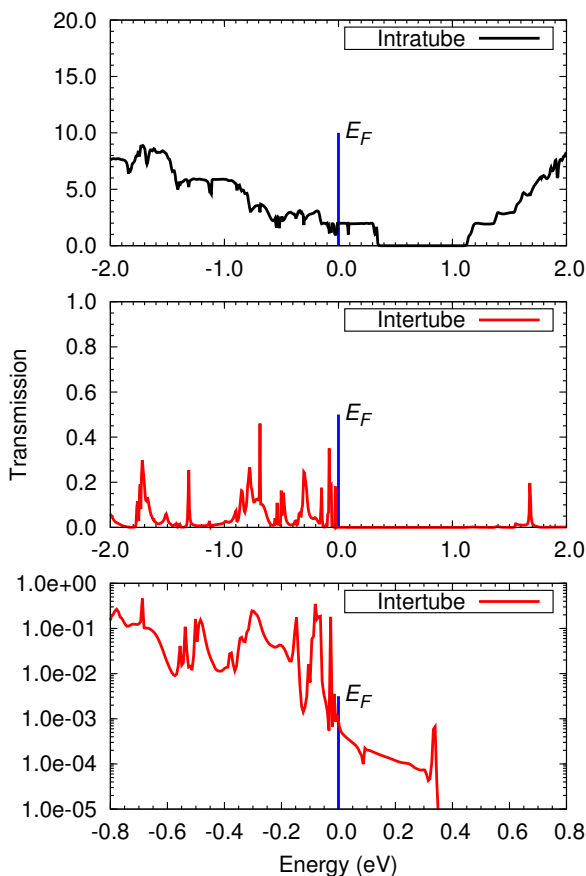


Figure 6.5. Intratube (top panel) and intertube (middle and bottom panels) electronic transmission functions for a junction of two AuCl_4 -doped (10,0) CNTs with a linking AuCl_4 anion. The Fermi level is located at the energy zero and is also denoted by a vertical blue line. The intertube transmission function on the logarithmic scale is presented in the bottom panel.

Computing the transmission functions for a junction of two perpendicular AuCl_4 -doped (10,0) CNTs that are also connected by a AuCl_4 anion shows clear improvements in the intra- and intertube conductivities relative to those obtained for a CNT junction system without doping. The top panel in Fig. 6.5 presents the intratube electronic transmission function for the CNT junction in Fig. 6.3(c). An upshift of the intratube transmission function occurs due to the doping, which means that the individual semiconducting (10,0) CNTs become metallic. However, there are numerous dips in the intratube function and they originate from scattering due to the AuCl_4 anions adsorbed on the CNTs. On the other hand, the dips do not decrease the intratube transmission markedly.

The most important finding of the transport calculations for the CNT junction system in Fig. 6.3(c) is that the electron transport through the junction enhances

significantly when the CNTs are doped with several anions and one anion bridges the CNTs. The intertube transmission functions in the middle and bottom panels of Fig. 6.5 reveal that the doping gives rise to a large number of peaks in a rather wide energy region and many of the peaks have values over 0.2. It should be noticed that the number of peaks in the intertube transmission function is very small at higher energies above the Fermi level. Further, the intratube transmission function possesses fewer dips in the high-energy regime. The low intertube conductivity above the Fermi energy in Fig. 6.5 can be attributed to the lack of molecular states. Besides these findings, another prominent property of the intertube transmission function for the junction of doped CNTs with a linking anion is the large density of the electronic states just below the Fermi level. These states are related to the hybridisation between the molecular and CNT ones. Furthermore, the Fermi level can be pinned to the van Hove singularity of the CNT as found in the case of the band structures of highly doped semiconducting (10,0) CNTs. This indicates stability of the doping effect with respect to the concentration of the anions in the system.

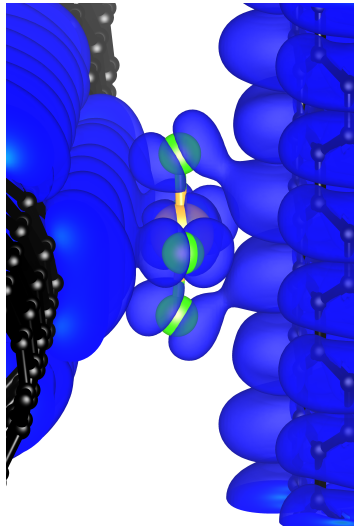


Figure 6.6. Total electron density of two double-degenerated states close to the Fermi level. The density has been computed for a model system consisting of two perpendicular (10,0) CNTs linked with a AuCl_4 anion.

It is also essential to explore the origin of the improvement of the intertube transmission functions for junctions comprising AuCl_4 -doped CNTs. In Publication II, we consider a model system that consists of two perpendicular pristine (10,0) CNTs connected by a AuCl_4 anion. We calculate the total electron densities of the electronic states lying near the Fermi level. Similarly to the studies of CNT junctions with TM linker atoms, we find hybridisation between the states of the CNT and those of the AuCl_4 anion. In Fig. 6.6, the total electron density of two states in the vicinity of the Fermi level is shown and the degeneracy of

the states is two.

The results of Publication II give insight into the doping of CNT networks with AuCl_3 on a molecular level. Moreover, our computational studies confirm the results of the work by Murat *et al.* [72] and indicate that the doping process stems from molecular AuCl_4 anions adsorbed on the CNTs. These anions always lead to a stable doping effect which increases significantly with increasing the concentration of the anions in the system. As it has been found in Ref. [72], the self-interaction of DFT causes an error in the band structures and this error can be reduced remarkably by including an atomistic self-interaction correction in the calculations. We have diminished the self-interaction error in our calculations by computing the band structures with the HSE06 hybrid exchange-correlation functional. The HSE06 calculations indicate higher charge transfer between the semiconducting CNTs and the adsorbed anion than in the same systems studied with the PBE functional.

An essential result of Publication II is also that the conductances of junctions of two semiconducting (10,0) CNTs without a linking anion improve significantly as a result of the AuCl_4 doping. The improvement already takes place when both CNTs in the junction are doped with a large enough concentration of anions. However, a larger value for the conductance is obtained when the doped CNTs are linked with a AuCl_4 anion. The conductance of the system increases in this case although the distance between the CNTs increases due to the linking anion. The findings related to the improvements of the junction conductances are in accordance with the experimental report where significant reductions in the sheet resistances of the CNT networks have been found [70, 47].

The downshift of the Fermi level in the band structure for a AuCl_4 -doped (10,0) CNT with a large molecular concentration is over 0.5 eV when performing the calculations with HSE06. This value is comparable to the experimental one, 0.42 eV [47]. Hence, achieving the downshift observed in the experiments requires a large concentration of AuCl_4 anions. Moreover, doping of graphene with AuCl_4 anions has also been examined computationally [73]. These studies indicate a significant increase in the work function accompanied by a clear downshift of the Fermi level. However, the shift of the Fermi level cannot be increased remarkably after reaching a saturation level. This effect may also occur in the case of CNTs and the Fermi level of the AuCl_4 -doped (10,0) CNTs cannot be shifted downwards in energy significantly if the concentration of the anions becomes large enough.

Graphene treated with AuCl_3 has also been investigated in Ref. [74] that shows how annealing of the sample affects the doping effect. The amounts of Au^{3+} and Cl^- ions in the system are found to vary according to the annealing temperature T_A . Their number is the largest at $T_A = 50^\circ\text{C}$. Then the resistance of the graphene sheet is also the lowest. Furthermore, an interesting finding of the work by Shin *et al.* is that the doping effect is reversible, which differs from the AuCl_3 -doped CNT systems.

Another study of graphene doped with AuCl_3 sheds light on the influence of

defects on the doping effect [75]. When the sample is irradiated with ultraviolet light, several types of defects form in the material and examples of these defects are oxygen-containing functional groups such as carbonyl groups and vacancies. The ultraviolet irradiation may change part of the sp^2 bonds to sp^3 ones. In Ref. [75], the irradiation time is optimised in order to find the largest conductivity of the CNT networks. An interesting issue related to this study is that the $AuCl_3$ doping works well even in the case of graphene with high density of defects. The suitability of the method for damaged graphene can be attributed to dangling bonds in the neighbourhood of the defects. These dangling bonds stabilise the chemical dopants. The influence of annealing and defects on $AuCl_3$ -doped graphene is considerable and these factors should be optimised when the graphene sheets are doped.

It has been shown in the work by Chang *et al.* [76] that a significant challenge related to the doping of graphene with $AuCl_3$ is the low charge transfer efficiency (CTE) between the dopant anions and graphene. The CTE depends remarkably on the sizes of the Au clusters that form during the doping process. The sizes of the Au clusters tend to become larger with increasing the dopant concentration, which results in higher values for CTE. However, to enhance the CTE drastically, the graphene sheet needs to be modified chemically. One way of improving the CTE is presented in Ref. [76]. First, a polymer layer is deposited on graphene and the entire system is heated. This step is followed by UV exposure, which introduces functional groups on the polymer layer. Thereafter, this structure is coated with $AuCl_3$. It turns out that the sheet resistance decreases at every step of the process in this case.

The factors that are associated with the efficiency of doping of graphene with $AuCl_3$ and are discussed in this section can also affect the performance of CNT thin films doped with $AuCl_4$ anions due to the similar atomic structure. It may be possible to tune and enhance the conductivity of $AuCl_4$ -doped CNT thin films by using ultraviolet radiation to make defects in them or by annealing them. An advantage of the annealing method is that it is simple to use. Furthermore, a chemical treatment like depositing appropriate polymer layers on CNT thin films can also be useful when the system is doped with $AuCl_4$ anions.

6.2 Carbon nanotubes with NO_3 molecules

The influence of nitric acid on CNTs can be studied by considering computational unit cells where nitrate molecules are adsorbed on semiconducting or metallic CNTs. In Publication III, several NO_3 -doped CNT systems are investigated in order to explore the doping effect. Part of the systems considered in Publication III are shown in Fig. 6.7. An example of the basic computational unit cell is shown in Fig. 6.7(a), where one NO_3 molecule resides on the system consisting of four primitive semiconducting (10,0) unit cells. Thus, the system is similar to that investigated in Publication II dealing with $AuCl_4$ -doped (10,0) CNTs.

Further, we also consider the computational unit cells of metallic (8,8) CNTs doped with NO_3 molecules. The system comprising seven primitive (8,8) unit cells with one NO_3 molecule on the outer surface is depicted in Fig. 6.7(c).

In addition, complexes containing NO_3 molecules coordinated to H_2O molecules and adsorbed on CNTs are also studied in Publication III. The CNT networks doped with nitric acid contain both H_2O and NO_3 molecules. Therefore, $\text{NO}_3\text{-H}_2\text{O}$ complexes can form in the NO_3 -doped CNT thin films. The system with only one $\text{NO}_3\text{-H}_2\text{O}$ complex is shown in Fig. 6.7(e). We also consider computational unit cells having a large concentration of NO_3 molecules or $\text{NO}_3\text{-H}_2\text{O}$ complexes and these systems are presented in Figs. 6.7(b), 6.7(d), and 6.7(f). In these cases, it is important to place the NO_3 molecules uniformly on the CNTs. The number of NO_3 molecules in the computational unit cells of Figs. 6.7(b) and 6.7(d) is eight. The last doped CNT in Fig. 6.7(f) is different from the two other systems with large numbers of molecules. There are two complexes above and below the CNT but the third complex is located on the sidewall. This way is chosen because of the simplicity of the configuration and the interaction between the complexes is still expected to remain low in this case.

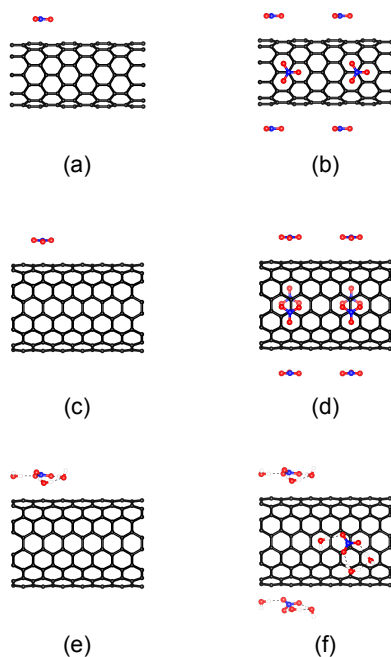


Figure 6.7. Computational unit cells of (a) a (10,0) CNT with one NO_3 molecule, (b) a (10,0) CNT with eight NO_3 molecules, (c) an (8,8) CNT with one NO_3 molecule, (d) an (8,8) CNT with eight NO_3 molecules, (e) an (8,8) CNT with one $\text{NO}_3\text{-H}_2\text{O}$ complex, and (f) an (8,8) CNT with three $\text{NO}_3\text{-H}_2\text{O}$ complexes.

Determining the adsorption geometry is an important part of the relaxation of the system. As there are a few possible sites on which the NO_3 molecule can

adsorb, testing each geometry separately could show the site with the lowest energy. We consider the binding energies for different adsorption geometries in the work by Peng *et al.* [77] and choose the configuration where the N atom of the molecule lies above the carbon atom and the oxygen atoms are above the centres of the carbon hexagons. The binding energy of this geometry is the lowest of all the four geometries examined in Ref. [77]. We only need to optimise the distance between the CNT and the NO_3 molecule $d_{\text{CNT-NO}_3}$ by relaxing the system. In the case of a semiconducting (10,0) CNT with one NO_3 molecule in the computational unit cell (see Fig. 6.7(a)), the distance $d_{\text{CNT-NO}_3}$ is 3.09 Å when the relaxation calculation includes the Tkatchenko-Scheffler van der Waals correction. For the metallic (8,8) CNT with one NO_3 molecule in the computational unit cell as presented in Fig. 6.7(c), the corresponding distance is 3.06 Å. The effect of a large molecular concentration on $d_{\text{CNT-NO}_3}$ is also examined in Publication III but this distance remains near the same value on average although the number of molecules is increased in the system.

The expression in Eq. (5.2) can be used to calculate the binding energy for one NO_3 molecule adsorbed on a semiconducting (10,0) CNT. For this system, the binding energy is -0.80 eV. Computing the binding energy for a similar system where one NO_3 molecule is on a metallic (8,8) CNT results in a larger value, -1.31 eV. The adsorption energy for the NO_3 molecule on a (10,0) CNT in Publication III is in good agreement with the corresponding value obtained in Ref. [78]. Moreover, the distances $d_{\text{CNT-NO}_3}$ in Publication III and in Ref. [78] are close to each other. An important remark of the study by Kroes *et al.* is that the binding energies for the NO_3 molecules are higher when they are adsorbed on metallic CNTs. Indeed, our values show similar behaviour. The higher binding energies for the NO_3 molecules on metallic CNTs can be explained by enhanced polarisation interaction. Furthermore, there is a dependence of the binding energy on the diameter and the band gap of the CNT [78]. For instance, the binding energy increases with increasing the diameter of the CNT. On the other hand, the binding energy is smaller for systems with larger band gaps. It turns out that the binding energy is remarkably larger in the case of metallic CNTs. In addition, the effect of the size of the CNT on the binding energy is relatively small if the CNT is metallic.

We also consider the band structures of NO_3 -doped CNTs in order to find the amount of charge transferred between the CNT and the adsorbed NO_3 molecules. The band structures for (a) a pristine semiconducting (10,0) CNT and (b)–(c) for semiconducting (10,0) CNTs with large numbers of NO_3 molecules are shown in Figs. 6.8(a)–(c). The calculations have been carried out using the PBE functional. The band structure for the pristine system in Fig. 6.8(a) is almost the same as Fig. 6.1(a). It can be seen from the band structure plot that the system is a semiconductor. Interestingly, the NO_3 molecules cause charge transfer from the CNTs to the molecules, which can be seen as a downshift of the Fermi level (see Figs. 6.8(b) and 6.8(c)). Dispersionless molecular states also appear just below the Fermi level in the band structure plots. The large number of states

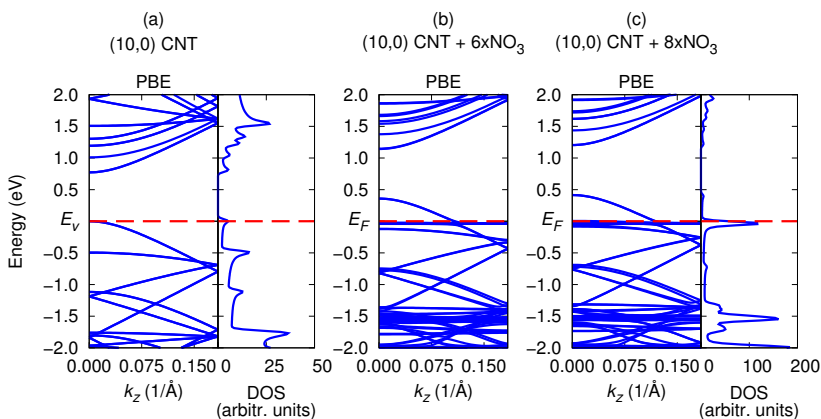


Figure 6.8. Band structures of (a) a pristine (10,0) CNT and (b)–(c) NO_3 -doped (10,0) CNTs. The number of NO_3 molecules in the computational unit cells of the doped systems is (b) six and (c) eight. In addition, the DOS is shown for the cases of a pristine (10,0) CNT and of a (10,0) CNT with eight NO_3 molecules in the computational unit cell. The top of the valence band and the Fermi level for the pristine system and for the NO_3 -doped systems, respectively, are denoted by red dashed lines. The band structures are computed with PBE.

is also shown by the DOS plot in Fig. 6.8(c). Another important remark is that the Fermi level lies in the proximity of the van Hove singularity. This indicates pinning of the Fermi level to the singularity as found in the case of AuCl_4 -doped (10,0) CNTs.

The band structure calculations presented in Figs. 6.8(a)–(c) have been carried out without spin. We also calculate the band structures for a computational unit cell comprising a (10,0) CNT with two adsorbed NO_3 molecules without and with spin as shown in Figs. 6.9(a) and 6.9(b), respectively. The influence of spin on the band structures can be seen as splitting of the dispersionless molecular states in the neighbourhood of the Fermi level. Except for this spin splitting, other bands in the -2.0 to 2.0 eV range overlap each other in the spin-polarised band structure in Fig. 6.9(b). The shift of the Fermi level changes a little when the calculation includes spin but the difference is small between the two cases.

The doping efficiency of the NO_3 molecules adsorbed on metallic (8,8) CNTs is also examined in Publication III by determining the band structures for computational unit cells with different molecular concentrations. Figures of the atomic structures of the NO_3 -doped CNT systems with a small and large molecular concentration are presented in Figs. 6.7(c) and 6.7(d), respectively. Furthermore, we consider other systems consisting of metallic (8,8) CNTs where the number of NO_3 molecules in the computational unit cell varies between one and eight. The band structure plots of metallic (8,8) CNTs without and with NO_3 molecules are shown in Figs. 6.10(a)–(c). If there are no NO_3 molecules on the (8,8) CNT, the band structure looks like that of a metal and the Fermi level is located at a point where two linear bands cross each other. The DOS for the

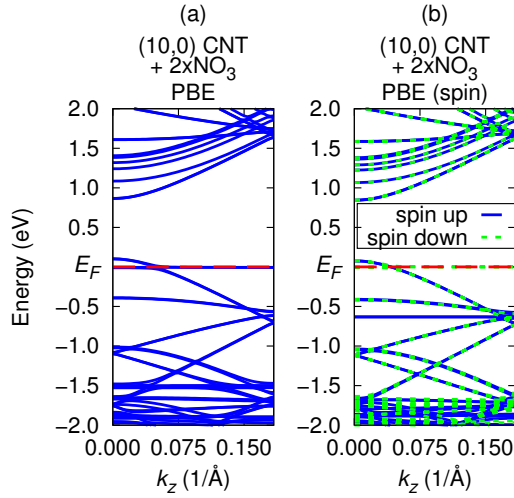


Figure 6.9. Band structures of a (10,0) CNT with two NO_3 molecules in the computational unit cell determined (a) without and (b) with spin-polarisation using PBE. The red dashed line represents the Fermi level.

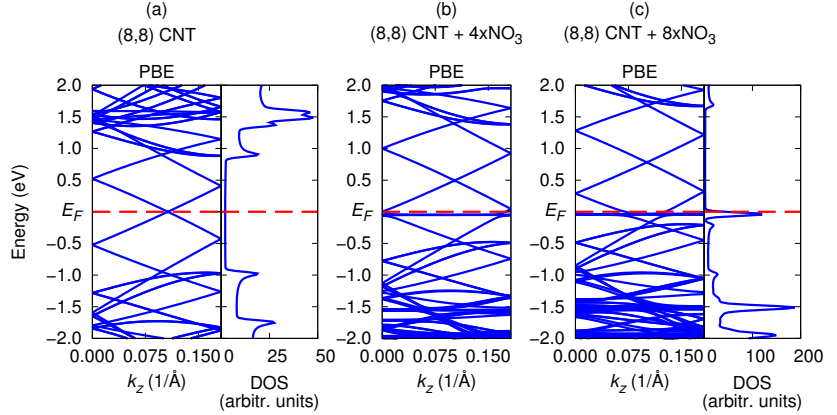


Figure 6.10. Band structures computed with PBE for (a) a pristine (8,8) CNT, (b)–(c) NO_3 -doped (8,8) CNTs. In the doped systems, the number of the NO_3 molecules in the computational unit cells is (b) four and (c) eight. Moreover, the DOS for a pristine CNT and for a CNT with eight NO_3 molecules in the computational unit cell are displayed.

same system reveals the positions of the van Hove singularities. Similarly to the band structures of NO_3 -doped semiconducting (10,0) CNTs, a downshift of the Fermi level can be observed in metallic (8,8) CNT systems when they are doped with NO_3 molecules (see Figs. 6.10(b) and 6.10(c)). If the computational unit cell of an (8,8) CNT has eight NO_3 molecules, the value of the downshift is

approximately 0.8 eV. In spite of the large downshift, the Fermi level does not shift so close to the van Hove singularity of the CNT and the band structure in Fig. 6.10(c) differs significantly from that shown in Fig. 6.8(c) where the Fermi level has fallen to the top of the valence band. Therefore, pinning of the Fermi level to the van Hove singularity is not expected to be so remarkable in the case of a NO_3 -doped metallic (8,8) CNT. However, the DOS just below the Fermi level in Fig. 6.10(c) is large and pinning of the Fermi level to this energy region with several molecular states seems to be possible if the bias voltage is small.

An important part of the band structure calculations is determining the doping efficiency of the adsorbed NO_3 molecules. The estimation of the transferred charge is performed using the same procedure as that used in the case of AuCl_4 -doped (10,0) CNTs. Thus, we search for the crossing points of the valence band and the Fermi level. This makes it possible to compute the charge transfer between the CNTs and the NO_3 molecules. The doping efficiencies for NO_3 -doped semiconducting (10,0) CNTs are given in Table 6.2. The corresponding values for metallic (8,8) CNTs doped with NO_3 molecules are listed in Table 6.3. The values of the doping efficiencies in Table 6.3 come from calculations where spin-polarisation has been ignored.

Table 6.2. Doping efficiency in NO_3 -doped semiconducting (10,0) CNTs per one adsorbed molecule. The values of this table have been computed with PBE and are given per molecule as a function of the number of NO_3 molecules (N_{NO_3}) in the computational unit cell.

| N_{NO_3} | Includes spin | Doping efficiency per NO_3 molecule (e) |
|-------------------|---------------|--|
| 1 | No | 0.6 |
| 2 | No | 0.5 |
| 2 | Yes | 0.4 |
| 6 | No | 0.4 |
| 8 | No | 0.3 |

Table 6.3. Doping efficiency in NO_3 -doped metallic (8,8) CNTs per one adsorbed molecule. The values determined with PBE are given as a function of the number of NO_3 molecules (N_{NO_3}) in the computational unit cell.

| N_{NO_3} | Doping efficiency per NO_3 molecule (e) |
|-------------------|--|
| 1 | 0.7 |
| 2 | 0.6 |
| 3 | 0.6 |
| 4 | 0.5 |
| 5 | 0.5 |
| 8 | 0.4 |

Approximately 0.6 electrons is transferred from the (10,0) CNT to the NO_3 molecule when there is only one molecule in the computational unit cell. With the same dopant concentration, the doping efficiency of the NO_3 molecule on a metallic (8,8) CNT is 0.7 electrons per molecule. In the case of both the doped semiconducting (10,0) CNT and doped metallic (8,8) CNT, the doping efficiency decreases as a function of the number of NO_3 molecules. If the number of molecules in the computational unit cell is increased to eight, the average doping efficiency decreases to 0.3 and 0.4 electrons per molecule for semiconducting (10,0) and metallic (8,8) CNTs, respectively. Hence, there are no big differences between the charge transfer values of semiconducting and metallic CNT systems. A spin-polarised calculation for the computational unit cell of a semiconducting (10,0) CNT with two NO_3 molecules shows that the spin has a negligible effect on the doping efficiency.

A well known problem associated with DFT is describing the charge transfer accurately. The problem arises from the self-interaction error that is included in all practical implementations of DFT. In Publication III, we also use the HSE06 hybrid exchange-correlation functional to diminish the self-interaction error. The same functional (HSE06) has been used to compute the band structures of AuCl_4 -doped (10,0) CNTs successfully in Publication II. Furthermore, Publication III also presents results from calculations that include the Perdew-Zunger self-interaction correction (SIC) and that have been carried out with the GPAW code package [79]. A comparison between the doping efficiencies calculated with the PBE functional, the HSE06 functional, and the Perdew-Zunger SIC method is made in Publication III. As the Perdew-Zunger SIC requires a system with a moderate size due to the computational cost, we consider a computational unit cell the length of which is half of the corresponding value of the standard unit cell displayed in Fig. 6.7(a). Besides testing the three aforementioned methods with the system in Fig. 6.7(a), another computational unit cell where a $\text{NO}_3\text{-H}_2\text{O}$ is placed on the short (10,0) CNT system is considered and the same three methods are also applied to this case.

The value of the molecular doping efficiency determined with PBE for the computational system comprising a (10,0) CNT and one adsorbed NO_3 molecule is 0.5 electrons. Using HSE06, a little higher value of 0.6 electrons is found. Interestingly, the charge transfer from the CNT to the NO_3 molecule is 0.9 electrons if the Perdew-Zunger SIC method along with the PW91 functional is used. Publication III also reveals that a similar trend can be seen in the doping efficiencies of $\text{NO}_3\text{-H}_2\text{O}$ complexes but the charge transfer values are significantly larger. The doping efficiency of the $\text{NO}_3\text{-H}_2\text{O}$ complex is found to be near one electron per complex when using the HSE06 functional. The same quantity computed with the Perdew-Zunger SIC is 1.1 electrons per complex. In Publication III, the charge transfer from the CNTs to the $\text{NO}_3\text{-H}_2\text{O}$ complexes is mainly explored using the HSE06 hybrid exchange-correlation functional because it gives charge transfer values that are closer to those computed with the Perdew-Zunger SIC method. The PBE functional, however, is used to perform

the electron transport calculations due to the low computational cost.

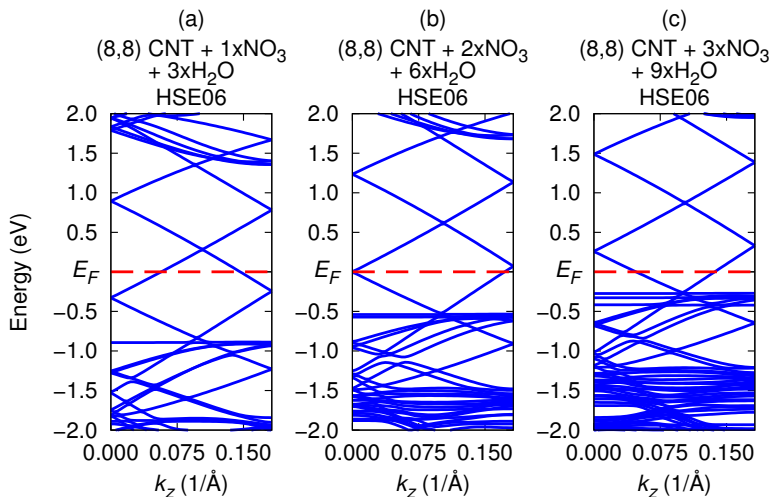


Figure 6.11. Plots of band structures for (8,8) CNTs with $\text{NO}_3\text{-H}_2\text{O}$ complexes. In the computational unit cell, the number of complexes is (a) one, (b) two, and (c) three. The functional in the calculations is HSE06.

The doping efficiency of $\text{NO}_3\text{-H}_2\text{O}$ complexes on metallic and semiconducting CNTs is also considered in Publication III. Band structures for systems consisting of metallic (8,8) CNTs with different numbers of $\text{NO}_3\text{-H}_2\text{O}$ complexes are determined and the results from these band structure calculations carried out with HSE06 are presented in Figs. 6.11(a)–(c). The most significant difference between the band structures of Fig. 6.11 and the doped systems in Fig. 6.8 is that the dispersionless molecular states that appear close to the Fermi level in Figs. 6.8(b) and 6.8(c) are remarkably shifted toward lower energies. Calculating the doping efficiency of a $\text{NO}_3\text{-H}_2\text{O}$ complex shows that the amount of charge transferred from the CNTs to the complexes is in each case approximately one electron per complex regardless of the concentration of the $\text{NO}_3\text{-H}_2\text{O}$ complexes.

6.3 Junctions of CNTs doped with NO_3 molecules

An essential topic of Publication III is electron transport through CNT junctions where the CNTs are doped with NO_3 molecules. As explained at the beginning of this chapter, three different model systems are investigated to understand the impact of the nitric acid on the conductances of the CNT junctions. The first system contains two NO_3 -doped semiconducting (10,0) CNTs and is depicted in Fig. 6.12(a). The concentration of NO_3 molecules on the CNTs is the same as that of the computational unit cell of a (10,0) CNT with the largest number of

NO_3 molecules. This computational unit cell has eight NO_3 molecules adsorbed on the CNT. A very similar system with the same dopant concentration is a junction of two NO_3 -doped metallic (8,8) CNTs and is shown in Fig. 6.12(b). The last junction contains two CNTs with different chiralities that are (8,8) and (10,0) and both CNTs are also doped with NO_3 molecules. A figure of this system is displayed in Fig. 6.12(c). This junction also differs from the other two systems where both CNTs have the same chiralities because the concentration of NO_3 molecules is not the same in the case of both CNTs although the difference is only two molecules per computational unit cell.

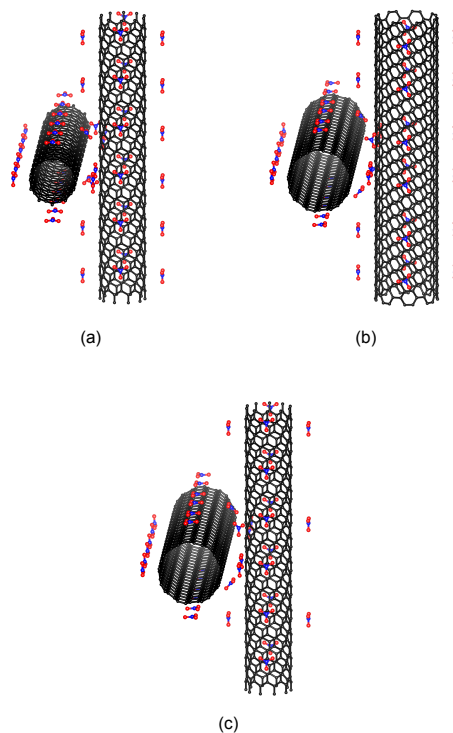


Figure 6.12. Junctions of (a) two NO_3 -doped (10,0) CNTs, (b) two NO_3 -doped (8,8) CNTs, and (c) NO_3 -doped (10,0) and NO_3 -doped (8,8) CNTs. The systems have a large dopant concentration.

The CNT junctions shown in Figs. 6.12(a)–(c) have been constructed using the computational unit cells of CNTs doped with NO_3 molecules. When adding a large number of molecules in the system, the positioning of the molecules causes a challenge particularly in the middle of the junction region. To avoid the interaction between the NO_3 molecules in the junction, part of them are moved along the surfaces of the CNTs so that the distance between the neighbouring molecules is sufficiently large. The relaxation calculations of junctions of AuCl_4 -doped (10,0) CNTs considered in Publication II revealed that optimising the

entire structure is a computationally demanding task. Hence, we only optimise the CNT-CNT distance in the three CNT junctions displayed in Figs. 6.12(a)–(c). This means that the positions of every atom in the system are fixed. We vary the distance between the CNTs and carry out a ground state calculation for each distance separately. Then, we can find the optimal distance by looking for the minimum of the total energy values.

Results from the optimisation of the CNT-CNT distances are given in Publication III and have been determined with the van der Waals correction. In the junction of two NO_3 -doped semiconducting (10,0) CNTs shown in Fig. 6.12(a), the optimised CNT-CNT distance is 3.21 Å. The corresponding values for the junction of two NO_3 -doped metallic (8,8) CNTs and for the junction of a semiconducting (10,0) CNT and a metallic (8,8) CNT doped with NO_3 molecules are 3.16 and 3.11 Å, respectively. These CNT-CNT distances are remarkably larger than the value found for a CNT junction without doping. For instance, the distance between two pristine (8,8) CNTs is between 2.5 and 2.6 Å, which is in agreement with Ref. [68] and with Publication I. The reason for the increase in the CNT-CNT distance is the charge transfer between the CNTs and the molecules and the ensuing enhanced Coulomb repulsion between the CNTs. On the other hand, the CNT-CNT distances do not depend on the chiralities of the CNTs significantly.

Examining the electronic transmission functions for junctions formed by two perpendicular NO_3 -doped CNTs gives insight into the effect of doping on the conductivity of the whole CNT network. The transport calculations for the junction that consists of two semiconducting (10,0) CNTs with large dopant concentrations and that is presented in Fig. 6.12(a) indicate that the doping results in a clear upshift of the intratube transmission curve. The plot of the actual transmission curve is not shown but it also has a few dips representing scattering. More specifically, there is a marked dip at the Fermi level and the dip is related to the dispersionless molecular states seen in the band structure figures. We can regard the dip near the Fermi level as a Fano antiresonance [80]. However, the conductivity along the CNT increases remarkably as a result of the NO_3 doping. Similarly, the intratube transmission curve for a junction of two NO_3 -doped metallic (8,8) CNTs (see Fig. 6.12(b)) shifts toward higher energies and possesses dips located both at the Fermi level and close to the edges of the steps below the Fermi level. The overall conductivity remains good in spite of the large molecular concentration on the CNT.

Interestingly, the adsorbed NO_3 molecules result in an enhancement of electron transport through the CNT junctions, which can be seen in the transmission functions presented in Figs. 6.13(a) and 6.13(b). In the case of a junction of two NO_3 -doped semiconducting (10,0) CNTs, at least two quite broad peaks arise near the Fermi energy as shown in Fig. 6.13(a). The first peak at the Fermi level is associated with the dispersionless molecular states whereas the second one comes from the van Hove singularity lying next to the molecular states. The other CNT junction consisting of similarly doped metallic (8,8) CNTs has an

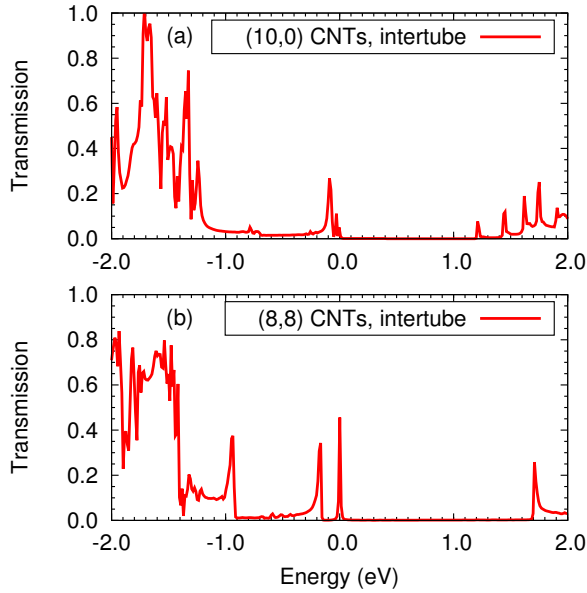


Figure 6.13. Intertube transmission functions for a junction of (a) two NO_3 -doped (10,0) CNTs and (b) two NO_3 -doped (8,8) CNTs. The Fermi level is located at the energy zero.

intertube transmission function (see Fig. 6.13(b)) where a sharp and high peak located at the Fermi level is found. This curve differs from that for the previous junction where the CNTs are originally semiconducting since the peak coming from the molecular states is so narrow.

The width of the van Hove singularity below the Fermi level in the intertube transmission function also increases because of the NO_3 doping, which can be stated by comparing the transmission plot in Figs. 6.13(a) with the corresponding intertube curve in Fig. 6.4. The widening of the peak indicates that there is hybridisation between the CNT and molecular orbitals. On the other hand, this kind of widening does not seem to be remarkable in the case of a junction of two NO_3 -doped metallic (8,8) CNTs as shown in Fig. 6.13(b). Examining the charge densities of the highest occupied eigenstates provides valuable information about the hybridisation in the system. Figures of the charge densities of the highest occupied eigenstates for doped semiconducting and metallic systems are presented in Figs. 6.14(a) and 6.14(b).

The hybridisation and spreading of the wavefunctions is larger in the NO_3 -doped semiconducting (10,0) CNT than in the similarly doped metallic (8,8) CNT, which can be verified by looking at Figs. 6.14(a) and 6.14(b). The enhanced hybridisation in the case of the NO_3 -doped semiconducting (10,0) system is also in agreement with the doping efficiencies computed for the same system. The values of the doping efficiencies are on average smaller when the molecules are adsorbed on the semiconducting CNTs than on the metallic ones. If the value



Figure 6.14. Charge density of the highest occupied eigenstate drawn for the computational unit cells for (a) a semiconducting (10,0) CNT with one NO_3 molecule and (b) a metallic (8,8) CNT with one NO_3 molecule.

of the charge transfer between the CNT and the NO_3 molecules is relatively small, then the formation of covalent bonds and strong hybridisation between the molecular orbitals are more probable in the system, which can be seen as enhanced coupling of the molecular orbitals in Figs. 6.14(a) and 6.14(b). The difference between these two figures explains why electron transport through a junction of doped semiconducting CNTs is higher than the electron transport through a system consisting of doped metallic CNTs.

Electron transport through the third junction formed by a NO_3 -doped metallic (8,8) CNT and a NO_3 -doped semiconducting (10,0) CNT is also investigated in Publication III. For this CNT junction system, the electronic transmission functions for intra- and intertube transport are shown in Fig. 6.15.

The conductivity along the CNTs with NO_3 doping in the third junction (see Fig. 6.12(c)) is displayed in the upper plot of Fig. 6.15 and the shapes of the transmission curves are characteristic of the intratube transmission functions obtained for individual CNTs or junctions of two CNTs with the same chiralities. In addition to the upshifts of the intratube transmission functions, a significant number of dips can be seen close to the steps of the curves and the intratube transmission functions of both doped CNTs have a dip located just at the Fermi level. The decrease in the electron transport at the Fermi level can be attributed to the Fano antiresonances as stated in the discussion of previous results.

The effect of NO_3 doping on the junction of doped semiconducting and metallic CNTs can be assessed by looking at the intertube transmission functions in the middle and lower plots in Fig. 6.15. There is a very narrow peak at the Fermi energy but the values of the intertube curve are very small in the neighbourhood of the peak. Further, the behaviour of the intertube transmission function is different from that computed for the two other CNT junctions with the same types of CNTs. Thus, the conductance of the last junction examined in Publication III is relatively low. The small values of the intertube transmission function and a small number of peaks in the curves come from different energy level structures of the NO_3 semiconducting and metallic CNTs. No peaks arise because the energy levels do not match. However, the NO_3 doping improves the conductance of the system a little and is necessary from the point of view of the conductivity of the entire CNT network.

In a former study of CNT networks with physisorbed O_2 and N_2 molecules, the conductance of different CNT junctions is investigated using both experimental

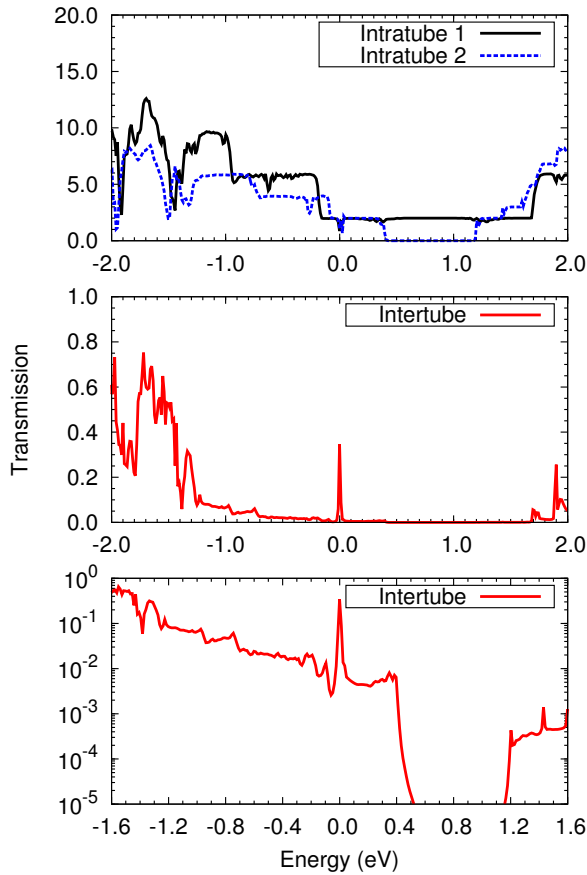


Figure 6.15. Intratube (upper plot) and intertube (middle and lower plots) electronic transmission functions for a junction consisting of an (8,8) and a (10,0) CNT that are also doped with NO_3 molecules. The number of NO_3 molecules in the computational unit cells of the (8,8) and (10,0) CNTs are eight and six, respectively. The bottom panel presents the intertube transmission function on the logarithmic scale.

techniques and first-principles electron transport calculations [81]. The results of Ref. [81] reveal that rather broad peaks arise in the intertube transmission functions for the junctions of two metallic or semiconducting CNTs with O_2 or N_2 molecules. The positions of the peaks correspond to the energies of the molecular orbitals. The first peaks originating from the highest-occupied molecular states are located at approximately 0.3 – 0.6 eV below the Fermi level. Furthermore, there are also significant increases in the intertube transmission functions at much lower and higher energies. The effect of these peaks on the conductance of the CNT junction, however, can be negligible because of the large distance between the peaks and the Fermi level. Moreover, the O_2 molecules are found to cause a larger enhancement of the junction conductance than the N_2 molecules. The influence of the physisorbed molecules is also larger on the junction of

semiconducting CNTs than on that of metallic CNTs [81], which is in agreement with the electron transport calculations of Publication III.

7. Conclusions

Two promising methods to improve the conductivity of CNT networks have been investigated computationally in this work. The first approach is based on linking the metallic CNTs with TM atoms. The second method involves AuCl_4 and NO_3 molecules that can dope the CNTs in the junctions and also act as linker molecules between two CNTs. These systems have been explored using DFT calculations. Both the basic geometries of the systems and their band structures have been considered. In order to study the conductances of CNT junctions, the standard Green's function method has been combined with DFT and four-terminal electronic transmission functions have been determined for various CNT junctions where the CNTs may be linked with molecules or TM atoms.

Electron transport through junctions of two perpendicular metallic CNTs can be greatly improved by linking the CNTs with TM atoms. The enhancement of the conductances of the CNT junctions does not seem to depend on the TM atom because all three TM linker atoms result in an equal increase in the conductance. In addition, the binding energies of TM linker atoms in the CNT junctions are negative, which indicates that the CNT junction systems are stable. The electron transport along one CNT is not significantly disturbed by the TM linker atom. Hence, connecting the CNTs with TM linker atoms is an appropriate way of improving the conductivity of CNT thin films. The key property of the CNT junction with a TM linker atom is the remarkable hybridisation between the carbon and TM atom orbitals, which enables the increase in the conductance of the CNT junction.

The latter part of this thesis deals with the molecular doping of CNTs and CNT junctions. Both AuCl_4 and NO_3 molecules cause charge transfer from the CNTs to the molecules indicating a p-type doping effect. Further, increasing the dopant concentration makes the Fermi level pin to the van Hove singularities and flat molecular states. The doping effect is more remarkable in the case of AuCl_4 molecules than in the NO_3 -doped CNT systems. The pinning effect is important in the improvement of the conductances of the CNT junctions. Moreover, the charge transfer increases when the NO_3 molecules are bound to H_2O molecules. The inclusion of self-interaction correction has also been

shown to be important in our studies. An increase in the conductance is found in the AuCl_4^- and NO_3^- -doped CNT junctions. In addition, the chiralities of the CNTs affect the increase in the conductance of the junction. The electron transport calculations for NO_3^- -doped systems show that the conductances of the CNT junctions increase more when the junctions are formed by two NO_3^- -doped semiconducting CNTs.

An advantage of the doping of CNTs with molecules is the simplicity of the method. However, another important issue in the doping is the stability. In real applications, the doping effect should remain high during a long time period. Furthermore, the electronic transmission functions computed for the CNT junctions do not include the effect of the bias voltage. Having a finite voltage in the CNT network can make the atoms, ions, and molecules migrate in the system, which may impact the performance of the device.

The present systems in this work consist of perpendicular single-walled CNTs. Therefore, the next studies could be related to junctions where the angle between the CNTs is different and the electronic transmission function is computed with a finite bias voltage. In addition, the model of our work is valid for networks of single CNTs. In real CNT thin films, the CNTs can also form bundles that cannot be studied so easily with our present model. However, our work gives insight into improving the electrical conductivity of CNT networks by using linker atoms or molecules and helps to understand the origin of the results of previous experimental reports. Doping of CNTs or linking them with TM atoms are promising methods to enhance the conductivities of CNT thin films.

References

- [1] M. F. L. De Volder, S. H. Tawfick, R. H. Baughman, and A. J. Hart. Carbon Nanotubes: Present and Future Commercial Applications. *Science* **339**, 535 (2013).
- [2] J. Zaumseil. Single-walled carbon nanotube networks for flexible and printed electronics. *Semiconductor Science and Technology* **30**, 074001 (2015).
- [3] D. S. Hecht, D. Thomas, L. Hu, C. Ladous, T. Lam, Y. Park, G. Irvin, and P. Drzaic. Carbon-nanotube film on plastic as transparent electrode for resistive touch screens. *Journal of the Society for Information Display* **17**, 941 (2009).
- [4] T. A. Shastry and M. C. Hersam. Carbon Nanotubes in Thin-Film Solar Cells. *Advanced Energy Materials* **7**, 1601205 (2017).
- [5] D. Zhang, K. Ryu, X. Liu, E. Polikarpov, J. Ly, M. E. Tompson, and C. Zhou. Transparent, Conductive, and Flexible Carbon Nanotube Films and Their Application in Organic Light-Emitting Diodes. *Nano Letters* **6**, 1880 (2006).
- [6] J. DeGraff, R. Liang, M. Q. Le, J.-F. Capsal, F. Ganet, and P.-J. Cottinet. Printable low-cost and flexible carbon nanotube buckypaper motion sensors. *Materials & Design* **133**, 47 (2017).
- [7] A. Pekker, M. Chen, E. Bekyarova, and R. C. Haddon. Photochemical generation of bis-hexahapto chromium interconnects between the graphene surfaces of single-walled carbon nanotubes. *Materials Horizons* **2**, 81 (2015).
- [8] B. B. Doudou, J. Chen, A. Vivet, and C. Poilâne. Ab initio study of chemical bond interactions between covalently functionalized carbon nanotubes via amide, ester and anhydride linkages. *Solid State Sciences* **53**, 56 (2016).
- [9] L. Duclaux. Review of the doping of carbon nanotubes (multiwalled and single-walled). *Carbon* **40**, 1751 (2002).
- [10] A. K. Manna and S. K. Pati. Doping single-walled carbon nanotubes through molecular charge-transfer: a theoretical study. *Nanoscale* **2**, 1190 (2010).
- [11] A. Wachi, H. Nishikawa, Y. Zhou, and R. Azumi. Stable iodide doping induced by photonic curing for carbon nanotube transparent conductive films. *Japanese Journal of Applied Physics* **57**, 065101 (2018).
- [12] H.-Z. Geng, K. K. Kim, K. P. So, Y. S. Lee, Y. Chang, and Y. H. Lee. Effect of Acid Treatment on Carbon Nanotube-Based Flexible Transparent Conducting Films. *Journal of the American Chemical Society* **129**, 7758 (2007).
- [13] R. M. Martin. *Electronic structure: basic theory and practical methods*. Cambridge University Press, Cambridge (2004).

- [14] P. Hohenberg and W. Kohn. Inhomogeneous Electron Gas. *Physicl Review* **136**, B864 (1964).
- [15] W. Kohn and L. J. Sham. Self-Consistent Equations Including Exchange and Correlation Effects. *Physical Review* **140**, A1133 (1965).
- [16] F. Herman, J. P. Van Dyke, and I. B. Ortenburger. Improved Statistical Exchange Approximation for Inhomogeneous Many-Electron Systems. *Physical Review Letters* **22**, 807 (1969).
- [17] J. P. Perdew and Y. Wang. Accurate and simple analytic representation of the electron-gas correlation energy. *Physical Review B* **45**, 13244 (1992).
- [18] J. P. Perdew, K. Burke, and M. Ernzerhof. Generalized Gradient Approximation Made Simple. *Physical Review Letters* **77**, 3865 (1996).
- [19] M. Grüning, A. Marini, and A. Rubio. Density functionals from many-body perturbation theory: The band gap for semiconductors and insulators. *The Journal of Chemical Physics* **124**, 154108 (2006).
- [20] J. Heyd, G. E. Scuseria, and M. Ernzerhof. Hybrid functionals based on a screened Coulomb potential. *The Journal of Chemical Physics* **118**, 8207 (2003).
- [21] A. V. Krukau, O. A. Vydrov, A. F. Izmaylov, and G. E. Scuseria. Influence of the exchange screening parameter on the performance of screened hybrid functionals. *The Journal of Chemical Physics* **125**, 224106 (2006).
- [22] C. Adamo and V. Barone. Toward reliable density functional methods without adjustable parameters: The PBE0 model. *The Journal of Chemical Physics* **110**, 6158 (1999).
- [23] J. M. Pérez-Jordá and A. D. Becke. A density-functional study of van der Waals forces: rare gas diatomics. *Chemical Physics Letters* **233**, 134 (1995).
- [24] K. Burke. Perspective on density functional theory. *The Journal of Chemical Physics* **136**, 150901 (2012).
- [25] Y. Andersson, D. C. Langreth, and B. I. Lundqvist. van der Waals Interactions in Density-Functional Theory. *Physical Review Letters* **76**, 102 (1996).
- [26] S. Grimme. Semiempirical GGA-type density functional constructed with a long-range dispersion correction. *Journal of Computational Chemistry* **27**, 1787 (2006).
- [27] A. Tkatchenko and M. Scheffler. Accurate Molecular Van Der Waals Interactions from Ground-State Electron Density and Free-Atom Reference Data. *Physical Review Letters* **102**, 073005 (2009).
- [28] V. Blum, R. Gehrke, F. Hanke, P. Havu, V. Havu, X. Ren, K. Reuter, and M. Scheffler. Ab initio molecular simulations with numeric atom-centered orbitals. *Computer Physics Communications* **180**, 2175 (2009).
- [29] J. D. Talman. Optimization of numerical orbitals in molecular MO-LCAO calculations. *International Journal of Quantum Chemistry* **95**, 442 (2003).
- [30] V. Havu, V. Blum, P. Havu, and M. Scheffler. Efficient O(N) integration for all-electron electronic structure calculation using numeric basis functions. *Journal of Computational Physics* **228**, 8367 (2009).
- [31] S. Datta. *Electronic Transport in Mesoscopic Systems*. Cambridge University Press, Cambridge (1995).
- [32] L. Yu, C. Shearer, and J. Shapter. Recent Development of Carbon Nanotube Transparent Conductive Films. *Chemical Reviews* **116**, 13413 (2016).

- [33] R. Saito, G. Dresselhaus, and M. S. Dresselhaus. *Physical Properties of Carbon Nanotubes*. Imperial College Press, London (1998).
- [34] S. Kumar, J. Y. Murthy, and M. A. Alam. Percolating Conduction in Finite Nanotube Networks. *Physical Review Letters* **95**, 066802 (2005).
- [35] D. Hecht, L. Hu, and G. Grüner. Conductivity scaling with bundle length and diameter in single walled carbon nanotube networks. *Applied Physics Letters* **89**, 133112 (2006).
- [36] M. Stadermann, S. J. Papadakis, M. R. Falvo, J. Novak, E. Snow, Q. Fu, J. Liu, Y. Fridman, J. J. Boland, R. Superfine, and S. Washburn. Nanoscale study of conduction through carbon nanotube networks. *Physical Review B* **69**, 201402(R) (2004).
- [37] A. Znidarsic, A. Kaskela, P. Laiho, M. Gaberscek, Y. Ohno, A. G. Nasibulin, E. I. Kauppinen, and A. Hassanien. Spatially Resolved Transport Properties of Pristine and Doped Single-Walled Carbon Nanotube Networks. *The Journal of Physical Chemistry C* **117**, 13324 (2013).
- [38] H. M. Tóháti, Á. Pekker, B. Á. Pataki, Z. Szekrényes, and K. Kamarás. Bundle versus network conductivity of carbon nanotubes separated by type. *The European Physical Journal B* **87**, 126 (2014).
- [39] P. N. Nirmalraj, P. E. Lyons, S. De, J. N. Coleman, and J. J. Boland. Electrical Connectivity in Single-Walled Carbon Nanotube Networks. *Nano Letters* **9**, 3890 (2009).
- [40] D. A. Jack, C.-S. Yeh, Z. Liang, S. Li, J. G. Park, and J. C. Fielding. Electrical conductivity modeling and experimental study of densely packed SWCNT networks. *Nanotechnology* **21**, 195703 (2010).
- [41] L.-P. Simoneau, J. Villeneuve, C. M. Aguirre, R. Martel, P. Desjardins, and A. Rochefort. Influence of statistical distributions on the electrical properties of disordered and aligned carbon nanotube networks. *Journal of Applied Physics* **114**, 114312 (2013).
- [42] R. Graupner, J. Abraham, A. Vencelová, T. Seyller, F. Hennrich, M. M. Kappes, A. Hirsch, and L. Ley. Doping of single-walled carbon nanotube bundles by Brønsted acids. *Physical Chemistry Chemical Physics* **5**, 5472 (2003).
- [43] C. Bower, A. Kleinhammes, Y. Wu, and O. Zhou. Intercalation and partial exfoliation of single-walled carbon nanotubes by nitric acid. *Chemical Physics Letters* **288**, 481 (1998).
- [44] W. Zhou, J. Vavro, N. M. Nemes, J. E. Fischer, F. Borondics, K. Kamarás, and D. B. Tanner. Charge transfer and Fermi level shift in *p*-doped single-walled carbon nanotubes. *Physical Review B* **71**, 205423 (2005).
- [45] H. Jeong and J.-Y. Park. Local Electrical Investigations of Nitric Acid Treatment Effects on Carbon Nanotube Networks. *The Journal of Physical Chemistry C* **119**, 9665 (2015).
- [46] D.-W. Shin, J. H. Lee, Y.-H. Kim, S. M. Yu, S.-Y. Park, and J.-B. Yoo. A role of HNO₃ on transparent conducting film with single-walled carbon nanotubes. *Nanotechnology* **20**, 475703 (2009).
- [47] K. K. Kim, J. J. Bae, H. K. Park, S. M. Kim, H.-Z. Geng, K. A. Park, H.-J. Shin, S.-M. Yoon, A. Benayad, J.-Y. Choi, and Y. H. Lee. Fermi Level Engineering of Single-Walled Carbon Nanotubes by AuCl₃ Doping. *Journal of the American Chemical Society* **130**, 12757 (2008).

- [48] S. L. Hellstrom, M. Vosgueritchian, R. M. Stoltenberg, I. Irfan, M. Hammock, Y. B. Wang, C. Jia, X. Guo, Y. Gao, and Z. Bao. Strong and Stable Doping of Carbon Nanotubes and Graphene by MoO_x for Transparent Electrodes. *Nano Letters* **12**, 3574 (2012).
- [49] K. Cui, Y. Qian, I. Jeon, A. Anisimov, Y. Matsuo, E. I. Kauppinen, and S. Maruyama. Scalable and Solid-State Redox Functionalization of Transparent Single-Walled Carbon Nanotube Films for Highly Efficient and Stable Solar Cells. *Advanced Energy Materials* **7**, 1700449 (2017).
- [50] A. A. Tonkikh, V. I. Tsebro, E. A. Obratsova, K. Suenaga, H. Kataura, A. G. Nasibulin, E. I. Kauppinen, and E. D. Obratsova. Metallization of single-wall carbon nanotube thin films induced by gas phase iodination. *Carbon* **94**, 768 (2015).
- [51] X. Fan, E. C. Dickey, P. C. Eklund, K. A. Williams, L. Grigorian, R. Buczko, S. T. Pantelides, and S. J. Pennycook. Atomic Arrangement of Iodine Atoms inside Single-Walled Carbon Nanotubes. *Physical Review Letters* **84**, 4621 (2000).
- [52] H.-P. Komsa, R. Senga, K. Suenaga, and A. V. Krasheninnikov. Structural Distortions and Charge Density Waves in Iodine Chains Encapsulated inside Carbon Nanotubes. *Nano Letters* **17**, 3694 (2017).
- [53] A. A. Eliseev, L. V. Yashina, N. I. Verbitskiy, M. M. Brzhezinskaya, M. V. Kharlamova, M. V. Chernysheva, A. V. Lukashin, N. A. Kiselev, A. S. Kumskov, B. Freitag, A. V. Generalov, A. S. Vinogradov, Y. V. Zubavichus, E. Kleimenov, and M. Nachtgeal. Interaction between single walled carbon nanotube and 1D crystal in CuX@SWCNT (X=Cl, Br, I) nanostructures. *Carbon* **50**, 4021 (2012).
- [54] V. I. Tsebro, A. A. Tonkikh, D. V. Rybkovskiy, E. A. Obratsova, E. I. Kauppinen, and E. D. Obratsova. Phonon contribution to electrical resistance of acceptor-doped single-wall carbon nanotubes assembled into transparent films. *Physical Review B* **94**, 245438 (2016).
- [55] L. Brownlie and J. Shapter. Advances in carbon nanotube n-type doping: Methods, analysis and applications. *Carbon* **126**, 257 (2018).
- [56] R. S. Lee, H. J. Kim, J. E. Fischer, A. Thess, and R. E. Smalley. Conductivity enhancement in single-walled carbon nanotube bundles doped with K and Br. *Nature* **388**, 255 (1997).
- [57] Y. Nonoguchi, M. Nakano, T. Murayama, H. Hagino, S. Hama, K. Miyazaki, R. Matsumura, M. Nakamura, and T. Kawai. Simple Salt-Coordinated n-Type Nanocarbon Materials Stable in Air. *Advanced Functional Materials* **26**, 3021 (2016).
- [58] T. Fukumaru, T. Fujigaya, and N. Nakashima. Development of n-type cobaltocene-encapsulated carbon nanotubes with remarkable thermoelectric property. *Scientific Reports* **5**, 7951 (2015).
- [59] S. Schneider, M. Brohmann, R. Lorenz, Y. J. Hofstetter, M. Rother, E. Sauter, M. Zharnikov, Y. Vaynzof, H.-J. Himmel, and J. Zaumseil. Efficient n-Doping and Hole Blocking in Single-Walled Carbon Nanotube Transistors with 1,2,4,5-Tetrakis(tetramethylguanidino)benzene. *ACS Nano* **12**, 5895 (2018).
- [60] P. W. Chiu, G. S. Duesberg, U. Dettlaff-Weglikowska, and S. Roth. Interconnection of carbon nanotubes by chemical functionalization. *Applied Physics Letters* **80**, 3811 (2002).
- [61] S. I. Cha, K. T. Kim, K. H. Lee, C. B. Mo, Y. J. Jeong, and S. H. Hong. Mechanical and electrical properties of cross-linked carbon nanotubes. *Carbon* **46**, 482 (2008).

- [62] S. Ozden, T. N. Narayanan, C. S. Tiwary, P. Dong, A. H. C. Hart, R. Vajtai, and P. M. Ajayan. 3D Macroporous Solids from Chemically Cross-linked Carbon Nanotubes. *Small* **11**, 688 (2014).
- [63] R. Kumari, P. K. Tyagi, and N. K. Puri. Electron irradiation induced wall-to-wall joining of multiwalled carbon nanotubes. *Applied Surface Science* **453**, 153 (2018).
- [64] I. Kalinina, E. Bekyarova, S. Sarkar, F. Wang, M. E. Itkis, X. Tian, S. Niyogi, N. Jha, and R. C. Haddon. Hexahapto-Metal Complexes of Single-Walled Carbon Nanotubes. *Macromolecular Chemistry and Physics* **213**, 1001 (2012).
- [65] X. Tian, M. L. Moser, A. Pekker, S. Sarkar, J. Ramirez, E. Bekyarova, M. E. Itkis, and R. C. Haddon. Effect of Atomic Interconnects on Percolation in Single-Walled Carbon Nanotube Thin Film Networks. *Nano Letters* **14**, 3930 (2014).
- [66] E. Y. Li and N. Marzari. Improving the Electrical Conductivity of Carbon Nanotube Networks: A First-Principles Study. *ACS Nano* **5**, 9726 (2011).
- [67] K. H. Khoo and J. R. Chelikowsky. Electron transport across carbon nanotube junctions decorated with Au nanoparticles: Density functional calculations. *Physical Review B* **79**, 205422 (2009).
- [68] P. Havu, M. J. Hashemi, M. Kaukonen, E. T. Seppälä, and R. M. Nieminen. Effect of gating and pressure on the electronic transport properties of crossed nanotube junctions: formation of a Schottky barrier. *Journal of Physics: Condensed Matter* **23**, 112203 (2011).
- [69] V. M. Rayón and G. Frenking. Bis(benzene)chromium Is a δ -Bonded Molecule and Ferrocene Is a π -Bonded Molecule. *Organometallics* **22**, 3304 (2003).
- [70] H. C. Choi, M. Shim, S. Bangsaruntip, and H. Dai. Spontaneous Reduction of Metal Ions on the Sidewalls of Carbon Nanotubes. *Journal of the American Chemical Society* **124**, 9058 (2002).
- [71] K. K. Kim, S. M. Kim, and Y. H. Lee. Chemically Conjugated Carbon Nanotubes and Graphene for Carrier Modulation. *Accounts of Chemical Research* **49**, 390 (2016).
- [72] A. Murat, I. Rungger, C. Jin, S. Sanvito, and U. Schwingenschlögl. Origin of the p-Type Character of AuCl₃ Functionalized Carbon Nanotubes. *The Journal of Physical Chemistry C* **118**, 3319 (2014).
- [73] H. Fang, R.-Z. Wang, and H. Yan. Work function modulation of AuCl₄⁻ molecule adsorbed on graphene: A first-principles simulation. *Chemical Physics Letters* **516**, 88 (2011).
- [74] D. H. Shin, J. M. Kim, C. W. Jang, J. H. Kim, S. Kim, and S.-H. Choi. Annealing effects on the characteristics of AuCl₃-doped graphene. *Journal of Applied Physics* **113**, 064305 (2013).
- [75] S. Oh, G. Yang, and J. Kim. AuCl₃ chemical doping on defective graphene layer. *Journal of Vacuum Science & Technology A: Vacuum, Surfaces, and Films* **33**, 021502 (2015).
- [76] K.-W. Chang, Y.-P. Hsieh, C.-C. Ting, Y.-H. Su, and M. Hofmann. Increasing the doping efficiency by surface energy control for ultra-transparent graphene conductors. *Scientific Reports* **7**, 9052 (2017).
- [77] S. Peng, K. Cho, P. Qi, and H. Dai. Ab initio study of CNT NO₂ gas sensor. *Chemical Physics Letters* **387**, 271 (2004).
- [78] J. M. H. Kroes, F. Pietrucci, K. Chikkadi, C. Roman, C. Hierold, and W. Andreoni. The response of single-walled carbon nanotubes to NO₂ and the search for a long-living adsorbed species. *Applied Physics Letters* **108**, 033111 (2016).

References

- [79] H. Gudmundsdóttir, E. Ö. Jónsson, and H. Jónsson. Calculations of Al dopant in α -quartz using a variational implementation of the Perdew–Zunger self-interaction correction. *New Journal of Physics* **17**, 083006 (2015).
- [80] C. J. Lambert. Basic concepts of quantum interference and electron transport in single-molecule electronics. *Chemical Society Reviews* **44**, 875 (2015).
- [81] D. J. Mowbray, C. Morgan, and K. S. Thygesen. Influence of O₂ and N₂ on the conductivity of carbon nanotube networks. *Physical Review B* **79**, 195431 (2009).



ISBN 978-952-60-8383-4 (printed)
ISBN 978-952-60-8384-1 (pdf)
ISSN 1799-4934 (printed)
ISSN 1799-4942 (pdf)

Aalto University
School of Science
Department of Applied Physics
www.aalto.fi

**BUSINESS +
ECONOMY**

**ART +
DESIGN +
ARCHITECTURE**

**SCIENCE +
TECHNOLOGY**

CROSSOVER

**DOCTORAL
DISSERTATIONS**